### Title

The origin of the unique achondrite Northwest Africa 6704: Constraints from petrology, chemistry and Re–Os, O and Ti isotope systematics




### Authors

Hibiya, Yuki
Archer, Gregory J
Tanaka, Ryoji
et al.



### Publication Date

2019

### DOI

10.1016/j.gca.2018.04.031

Peer reviewed

Published in final edited form as:
*Geochim Cosmochim Acta*. 2019 January 15; 245: 597–627. doi:10.1016/j.gca.2018.04.031.

# The origin of the unique achondrite Northwest Africa 6704: Constraints from petrology, chemistry and Re–Os, O and Ti isotope systematics

**Yuki Hibiya**[a,*], **Gregory J. Archer**[b,c], **Ryoji Tanaka**[d], **Matthew E. Sanborn**[e], **Yuya Sato**[f], **Tsuyoshi Iizuka**[a], **Kazuhito Ozawa**[a], **Richard J. Walker**[b], **Akira Yamaguchi**[g,h], **Qing-Zhu Yin**[e], **Tomoki Nakamura**[f], and **Anthony J. Irving**[i]

[a] Department of Earth and Planetary Science, University of Tokyo, Hongo 7-3-1, Bunkyo, Tokyo 113-0033, Japan

[b] Department of Geology, University of Maryland, College Park, MD 20742, USA

[c] Institut für Planetologie, University of Münster, Wilhelm-Klemm-Straße 10, 48149 Münster, Germany

[d] The Pheasant Memorial Laboratory for Geochemistry and Cosmochemistry, Institute for Planetary Materials (IPM), Okayama University, Misasa, Tottori 682-0193, Japan

[e] Department of Earth and Planetary Sciences, University of California-Davis, One Shields Avenue, Davis, CA 95616, USA

[f] Laboratory for Early Solar System Evolution, Division of Earth and Planetary Materials Science, Graduate School of Science, Tohoku University, Aoba, Sendai, Miyagi 980-8578, Japan

[g] National Institute of Polar Research, 10-3, Midori-cho, Tachikawa-shi, Tokyo 190-8518, Japan

[h] Department of Polar Science, School of Multidisciplinary Science, SOKENDAI (The Graduate University for Advanced Studies), Tokyo 190-8518, Japan

[i] Department of Earth and Space Sciences, University of Washington, Seattle, WA, USA

## Abstract

Northwest Africa (NWA) 6704 is a unique achondrite characterized by a near-chondritic major element composition with a remarkably intact igneous texture. To investigate the origin of this unique achondrite, we have conducted a combined petrologic, chemical, and $^{187}Re$–$^{187}Os$, O, and Ti isotopic study. The meteorite consists of orthopyroxene megacrysts ($En_{55–57}Wo_{3–4}Fs_{40–42}$; Fe/Mn = 1.4) up to 1.7 cm in length with finer interstices of olivine ($Fa_{50–53}$; Fe/Mn = 1.1–2.1), chromite (Cr# ~ 0.94), awaruite, sulfides, plagioclase ($Ab_{92}An_5Or_3$) and merrillite. The results of morphology, lattice orientation analysis, and mineral chemistry indicate that orthopyroxene megacrysts were originally hollow dendrites that most likely crystallized under high super-saturation and super-cooling conditions (1–$10^2$ °C/h), whereas the other phases crystallized

* Corresponding author. yuki-hibiya@eps.s.u-tokyo.ac.jp (Y. Hibiya).

APPENDIX A. SUPPLEMENTARY DATA

Supplementary data associated with this article can be found, in the online version, at https://doi.org/10.1016/j.gca.2018.04.031.

between branches of the dendrites in the order of awaruite, chromite → olivine → merrillite → plagioclase. In spite of the inferred high supersaturation, the remarkably large size of orthopyroxene can be explained as a result of crystallization from a melt containing a limited number of nuclei that are preserved as orthopyroxene megacryst cores having high Mg# or including vermicular olivine. The Re–Os isotope data for bulk and metal fractions yield an isochron age of 4576 ± 250 Ma, consistent with only limited open system behavior of highly siderophile elements (HSE) since formation. The bulk chemical composition is characterized by broadly chondritic absolute abundances and only weakly fractionated chondrite-normalized patterns for HSE and rare earth elements (REE), together with substantial depletion of highly volatile elements relative to chondrites. The HSE and REE characteristics indicate that the parental melt and its protolith had not undergone significant segregation of metals, sulfides, or silicate minerals. These combined results suggest that a chondritic precursor to NWA 6704 was heated well above its liquidus temperature so that highly volatile elements were lost and the generated melt initially contained few nuclei of relict orthopyroxene, but the melting and subsequent crystallization took place on a timescale too short to allow magmatic differentiation. Such rapid melting and crystallization might occur as a result of impact on an undifferentiated asteroid. The O–Ti isotope systematics ($\Delta^{17}O = -1.052 \pm 0.004$, 2 SD; $\varepsilon^{50}Ti = 2.28 \pm 0.23$, 2 SD) indicate that the NWA 6704 parent body sampled the same isotopic reservoirs in the solar nebula as the carbonaceous chondrite parent bodies. This is consistent with carbonaceous chondrite-like refractory element abundances and oxygen fugacity (FMQ = −2.6) in NWA 6704. Yet, the Si/Mg ratio of NWA 6704 is remarkably higher than those of carbonaceous chondrites, suggesting significant nebular fractionation of forsterite in its provenance.

**Keywords**

NWA 6704; Primitive achondrite; Nucleosynthetic anomalies; Highly siderophile elements; Impact melting

## 1. INTRODUCTION

A fundamental and long-standing issue in planetary science is determining when, where, and how asteroids formed and differentiated (e.g., Ringwood 1961; Anders and Goles 1961; Mason 1967; Weiss and Elkins-Tanton, 2013; Day, 2015). Information regarding this must come from meteorites that record the early histories of their respective asteroidal parent bodies. Primitive achondrites are meteorites that have near-chondritic bulk compositions, but exhibit igneous and/or metamorphic textures (Prinz et al., 1980, 1983; Benedix et al., 1998; Weisberg et al., 2006; Rubin, 2007). They include several meteorite groups such as acapulcoites, lodranites, and winonaites (Weisberg et al., 2006; Greenwood et al., 2012). These meteorites record variable stages in the transition from chondrites to differentiated achondrites, from high degrees of metamorphism and anatexis of chondritic protoliths (acapulcoites and winonaites, e.g., Mittlefehldt et al., 1996; McCoy et al., 1996; Benedix et al., 1998; Floss et al., 2008), to various degrees of partial melting and melt extraction (lodranites as well as ureilites and brachinites, e.g., Goodrich, 1992; Mittlefehldt et al., 1996; Rubin, 2006; Warren et al., 2006; Keil, 2014). Moreover, shared O isotopic compositions and other similarities suggest that acapulcoites–lodranites and winonaites–IAB

complex iron meteorites may share common parent bodies, respectively (e.g., McCoy et al., 1993; Benedix et al., 1998, 2005; Floss et al., 2008). Thus, primitive achondrites provide an important opportunity to bridge the gap between chondrites and differentiated achondrites, and to decipher the thermal histories of (partially) undifferentiated planetesimals.

Recently, it has been found that several ungrouped achondrites, that are not classified into any known meteorite groups, also have near-chondritic major element compositions together with prominent igneous textures (e.g., Day et al., 2009, 2015; Gardner-Vandy et al., 2012; Warren et al., 2013). Such ungrouped achondrites are of importance for investigating the diversity of asteroids, and for refining our current understanding of early solar system evolution gained from grouped achondrites. Studies of ungrouped achondrites, however, are limited.

Northwest Africa (NWA) 6704 is an ungrouped achondrite found in Algeria in 2010, with a total known weight of 8.387 kg (Le Corre et al., 2014). NWA 6704 has rounded shiny surfaces with one small patch of remnant black fusion crust (Fig. 1). Its interior exhibits an igneous texture with no diagnostic shock deformation effects (Irving et al., 2011). The degree of weathering is restricted to minor coatings of orange dust on broken surfaces (Le Corre et al., 2014). NWA 6704 is composed of low-Ca pyroxene, less abundant Ni-rich olivine, plagioclase, chromite, Ni-Fe-metal (awaruite), sulfides (heazlewoodite and pentlandite) and merrillite (Irving et al., 2011; Le Corre et al., 2014). Initial studies indicated its bulk major element composition is nearly chondritic (Fernandes et al., 2013). The geochemical and petrological similarities suggest that NWA 6704 is paired with NWA 6693 and NWA 6926 (Warren et al., 2013). U–Pb dating for acid-washed pyroxene of NWA 6704 has yielded a Pb-Pb isochron age of 4562.46 ± 0.35 Ma with a measured $^{238}U/^{235}U$ ratio of 137.7784 ± 0.0097 (Amelin et al., 2019). The pristine characteristics of NWA 6704, coupled with its early crystallization age, make it ideal for exploring the earliest stage of asteroid evolution.

In this study, we present petrologic observations, geochemistry including highly siderophile element (HSE: Re, Os, Ir, Ru, Pt, Pd) abundances, $^{187}Re–^{187}Os$ systematics, and O–Ti isotope systematics for NWA 6704. The results allow us to constrain the crystallization process of this unique achondrite and the nature and provenance of the parental body.

## 2. METHODS

### 2.1. Petrology

We prepared nine polished thin sections from four fragments of NWA 6704 for petrologic studies, (Table 1; TS-1 and −2 from fragment #1, TS-3–5 from fragment #2, TS-6 and −8 from fragment #3, and TS-7 and −9 from fragment #4). Petrologic analyses were carried out by means of optical and electron microscopies at the University of Tokyo and National Institute of Polar Research, Japan. Optical microscopy was performed using a *Nikon ECLIPSE E600W* polarizing optical microscope equipped with *Axiocam-MR* camera and *Axiovision 4* software. More detailed observation was conducted using a *JEOL JXA-7000F* field emission-scanning electron microscope equipped with an energy dispersive spectrometer (FE-SEM/EDS). Analytical conditions were 15 kV accelerating voltage, 10

mm working distance, and 12 nA specimen current. Major element compositions of minerals were determined using a *JEOL JXA-8530L* electron probe micro analyzer (EPMA) with 15–25 kV accelerating voltages, 11 mm working distance, and 12–20 nA specimen currents. Elemental maps were acquired for the four thin sections (TS-6–9) using *JEOL JXA-8900L* EPMA with 15 kV accelerating voltages and 80 nA specimen current. The entire thin sections of TS-6 and TS-7 were mapped for characterization of their textural features and determination of modal abundances. Crystallographic orientations in the two thin sections were further investigated by FE-SEM combined with an electron back-scattering diffraction (EBSD) detector (*JEOL JSM 7000F* and *7100F* FE-SEM/EBSD) with the *HKL Channel-5* data acquisition and processing software. The EBSD technique allows us to determine the crystallographic orientations from Kikuchi patterns regardless of mineral phase contents (Schwartz et al., 2009). The instruments were operated at an accelerating voltage of 15 kV, a working distance of 25 mm, and a beam current of 10nA. Orientation maps were created for orthopyroxene by scanning the sample (108–200 μm step), in which orientations are coded according to Euler color. Pole figure diagrams for {1 0 0} of orthopyroxene were obtained by processing the data. To characterize the spatial distribution of minerals in NWA 6704, we performed micro X-ray computed tomography (CT) using a ScanXmate-D180RSS270 at Tohoku University, Japan. A sample chip of NWA 6704 (2.4 × 12.4 × 16.7 mm) was scanned using an X-Ray beam at 130 kV and 120 μA, with isotropic voxels (3-D pixels) of 12.093 μm. X-rays were filtered with 1 mm copper filter. We used a Thermo Fisher Scientific™ Amira™ 6.0 reconstruction software to recreate 3D images from the obtained 600–1600 2D slice images.

### 2.2. Major and trace element geochemistry

For major element geochemistry, a ~4 g fragment of NWA 6704 (fragment #5) was disaggregated using an agate mortar and pestle. Approximately 200 mg of the sample powder was fused in a mixture of sample powder and $Li_2$-$B_4O_7$ to form a glass disk, on which the major element abundance determination was carried out using a Thermo-ARL Advant'XP + sequential X-ray fluorescence (XRF) spectrometer at the Washington State University (WSU) Geoanalytical Laboratory. Major elements were normalized on a volatile-free basis with total Fe expressed as FeO.

For solution-based bulk and mineral chemistry measurement, two fusion-crust free subsamples of NWA 6704 (fragment #3: 678 mg, fragment #6: 42.9 mg) were powdered in an agate mortar and pestle. In addition to NWA 6704, an aliquot of NWA 6693 (39.5 mg) was also prepared for bulk chemistry measurement. Four powdered whole rock fractions of NWA 6704 (50.2 mg, 50.1 mg, 51.6 mg aliquots of fragment #3-a,b,c, and whole aliquot of fragment #6) and the NWA 6693 aliquot were digested with a concentrated 3:1 HF–$HNO_3$ mixture in a Parr® digestion bomb at 190 °C for 96 h. Besides, plagioclase and orthopyroxene mineral separates of NWA 6704 were digested a concentrated 3:1 HF–$HNO_3$ mixture on a hot plate. Digestion was followed by a treatment with alternating solution of 6 M HCl and concentrated $HNO_3$ for conversion to a soluble form. Aliquots of fragment #3 were diluted by a factor of 500 in 0.5 M $HNO_3$ for trace elements using a Thermo Fisher Scientific™ iCAP Q™ ICP–MS at the University of Tokyo. Aliquots of NWA 6704-fragment #6 and mineral separates and NWA 6693 were diluted in 2% $HNO_3$ for trace/minor

and major elements using a *Thermo Fisher Scientific Element XR* high-resolution inductively coupled plasma mass spectrometer (ICP-MS) at the University of California at Davis. Sample dilution factors were 4500 and 95,000 for trace/minor and major elements, respectively. Analyses were made in low-, medium-, or high-resolution, based on the resolution conditions needed for a given element. The accuracy was evaluated by analyzing well-characterized terrestrial rock standards (BHVO-2 and JB-1b) and Murchison meteorite dissolved in the same manner as NWA 6704. These results are reported in Table EA-1 together with literature values (Jarosewich, 1971; Terashima et al., 1998; Friedrich et al., 2002; Makishima and Nakamura, 2006; Jochum et al., 2015; Kon and Hirata, 2015).

### 2.3. Highly siderophile element and Re–Os isotope analysis

Four bulk fragments as well as a non-magnetic and magnetic separates were analyzed for highly siderophile element abundances (Re, Os, Ir, Ru, Pt, Pd) and $^{187}Re$–$^{187}Os$ isotope systematics. Approximately 70 mg of bulk fragments and a non-magnetic (primarily silicate) fraction were crushed into fine powders using an agate mortar and pestle. The magnetic fraction, containing mostly FeNi-rich metal, could not be crushed, and was dissolved as whole grains. Samples were combined with ~5 mL of a 2:1 mixture of Teflon distilled, concentrated $HNO_3$ and HCl, and appropriate amounts of two isotopic spikes, one enriched in $^{185}Re$ and $^{190}Os$, the other enriched in $^{191}Ir$, $^{99}Ru$, $^{194}Pt$, and $^{105}Pd$. Samples, spikes, and acids were sealed in 8 mL *Pyrex*™ Carius tubes (Shirey and Walker, 1995) and heated at 260 °C for three days. After digestion, Os was extracted from the acid by solvent extraction using $CCl_4$, and back extraction into concentrated HBr (Cohen and Waters, 1996). The Os was then purified using a microdistillation technique from a dichromate solution into concentrated HBr (Birck et al., 1997). The remaining HSE (Re, Ir, Ru, Pt, and Pd) were separated and purified via anion exchange chromatography using 10 mL *Bio-Rad* columns loaded with ~1 mL of AG1-X8 anion exchange resin (Rehkämper and Halliday, 1997).

Purified Os was analyzed by negative thermal ionization mass spectrometry (N-TIMS) on either the University of Maryland (UMd) *VG Sector 54* or *Thermo-Fisher Triton* using Faraday cups. The Os solutions were dried onto Pt filaments and then a $Ba(OH)_2$ activator was added (Creaser et al., 1991). The other HSE were analyzed as solutions by multicollector-ICP-MS (MC-ICP-MS) on the *Nu Plasma* at University of Maryland (UMd) using Faraday cups. The measurements of Ir, Ru, Pt, and Pd were corrected for mass bias by interspersing standards with sample measurements. Tungsten was added to Re fractions and mass bias corrections were made using $^{184}W/^{186}W = 1.0780$ (Kleine et al., 2004).

Mean (N = 2) blanks were 1.3 ± 1.3 pg for Re, 1.6 ± 0. 8 pg for Os, 0.7 ± 0.4 pg for Ir, 2.3 ± 0.3 pg for Ru, 4.3 ± 4.0 pg for Pt, and 4.6 ± 4.6 pg for Pd. The Os blank correction was 1.4% for the silicate fraction, and less than 0.12% for all other fractions. Blank corrections of Re, Pt, and Pd were 2.6%, 3.9%, and 1.5%, respectively, for the silicate fraction. All other blank corrections, including Ir and Ru blank corrections for the silicate fraction, were less than 0.1%. Uncertainties arising from blank corrections are included in reported uncertainties. The total uncertainties for Ir, Ru, Pt, and Pd concentrations of bulk and magnetic fractions are ≤1%. For the Re and Os concentrations of bulk and magnetic

fractions, uncertainties are less than 0.2% and 0.1%, respectively. The total uncertainties for HSE concentrations of silicate fractions are all less than 5%.

### 2.4. Oxygen isotope analysis

A ~550 mg fragment of NWA 6704 was crushed in a silicon nitride mortar and pestle, then sieved. The grain size of constituent minerals of NWA 6704 ranged up to centimeter length. To reduce the heterogeneity in the mineral proportion among the analyzed sample aliquots, a mineral fraction of 73–120 μm in diameter was used for the analyses. The fraction was washed in high purity water three times and dried at 80 °C overnight. After drying, metal grains were magnetically removed from the fractions. Since no weathered material was identified in the separated fraction under the microscope, no further cleaning was performed.

The O isotope analyses were conducted on five separates using the fluorination and gas purification methods modified after Sharp (1990) at the Institute for Planetary Materials, Okayama University. Details of the method are described in Tanaka and Nakamura (2013) and Pack et al. (2016). About 1–2 mg of sample was placed in a Ni sample holder. To remove the absorbed moisture, the sample was baked at 170 °C for 6 h *in vacuo*, then prefluorinated with $BrF_5$ for 1 h before analysis. The $O_2$ was extracted from each sample using a $CO_2$ laser (*PIN-10R*, Onizca Glass, Japan) with $BrF_5$ as oxidation agent. Extracted oxygen was then purified and trapped with 13 Å molecular sieve at liquid nitrogen temperature. Total procedural $O_2$ blanks for the laser fluorination method were typically <20 ppm relative to the sample gas. Thus, no blank correction was performed. The isotope ratios in the purified $O_2$ gases were determined using a *Thermo Finnigan* MAT253 gas source mass spectrometer with the dual inlet mode. Each sample measurement comprised 8 blocks of 11 cycles with a total measurement time of ~90 min. The $^{18}O/^{16}O$ and $^{17}O/^{16}O$ of the samples are expressed as the common delta (δ) notation relative to VSMOW as $\delta^{17 \text{ or } 18}O = 10^3 \times [(^{17 \text{ or } 18}O/^{16}O)_{sample}/(^{17 \text{ or } 18}O/^{16}O)_{VSMOW} - 1]$ using a VSMOW-SLAP scale. The excess $^{17}O$ values relative to terrestrial silicate fractionation line (TSFL) are defined as $\Delta^{17}O = 10^3 \times [\ln(\delta^{17}O^* \times 10^{-3} + 1) - 0.527 \times \ln(\delta^{18}O \times 10^{-3} + 1)]$, where $\delta^{17}O^* = \delta^{17}O + 0.039$ (Tanaka and Nakamura, 2013; Pack et al., 2016). Since most of the laboratories for O isotope analysis do not calibrate the working gas by VSMOW-extracted oxygen, it is widely assumed that the $\Delta^{17}O$ value of VSMOW is the same as that of the so-called terrestrial fractionation, i.e. $\Delta^{17}O = 0$, (Tanaka and Nakamura, 2013). The $\delta^{17}O^*$ value defined in this study corresponds to the $\delta^{17}O$ value so far published by other laboratories unless otherwise mentioned. The precision and accuracy during the course of this study were monitored by analyzing the San Carlos olivine (MSOL-1), which yielded $\delta^{18}O = 5.246 \pm 0.066$, $\delta^{17}O^* = 2.762 \pm 0.036$, and $\Delta^{17}O = 0.001 \pm 0.010$ (N = 5, 2 SD).

### 2.5. Titanium isotope analysis

For Ti isotope analysis, we used *ca*. 300 chromite grains, which were hand-picked from a medium-grain fraction (60–350 μm in diameter) of NWA 6704 under the stereoscopic microscope. Two chromite aliquots were separately washed in distilled acetone and digested with ~1 mL of concentrated HF + $HNO_3$ + $HClO_4$ with a volume ratio of 20:10:1 in a *Parr*® bomb at 190 °C for 2 days. The digested samples were converted from insoluble fluorides to

soluble compounds by repeated evaporation with concentrated $HNO_3$ + $HClO_4$, and finally re-dissolved in 2 mL of 6 M HCl.

For accurate and precise determinations of Ti isotope compositions, the purification of Ti was required to avoid matrix effects and isobaric interferences of Ca, V and Cr during the measurements. Our samples were processed through a three-step ion-exchange procedure based on Yamakawa et al. (2009), Zhang et al. (2011), and Schiller et al. (2014). In the first step, the sample dissolved in 2 mL of 6 M HCl was loaded onto a column packed with AG1-X8 anion resin (200–400 mesh), in which Ti and most matrix elements were eluted, while Fe was retained by the resin. The elution was dried down and re-dissolved in 3 mL of 0.5 M $HNO_3$, which was then loaded onto a column containing AG50W-X8 cation resin (200–400 mesh). In the second-step, most matrix elements including Ca, Cr, and V were removed with 0.5 M $HNO_3$ and 1.8 M HCl, and then Ti was collected with 0.5 M HF. The Ti fraction was dried down and re-dissolved in 3 mL of 12 M $HNO_3$ for the third step using *Eichrom* prepacked 2 mL cartridges containing TODGA resin (200–400 mesh). The third step removed residual Ca, Cr and V with 12 M $HNO_3$, and Ti was collected with 12 M $HNO_3$ + 1% $H_2O_2$.

The Ti isotopic compositions were measured using a *Thermo Fisher Scientific Neptune Plus* MC-ICP-MS interfaced to a *Cetac Aridus II* desolvating nebulizer at the University of Tokyo. The measurements were conducted using a Jet sample cone and a skimmer H-cone in the high-resolution mode, which resulted in a typical sensitivity for Ti of 60–70 $V \cdot ppm^{-1}$ ($10^{11}$ Ω resistor). Data were acquired with dynamic mode on Faraday cups to monitor species $^{44}Ca^+$, $^{91}Zr^{2+}$, $^{46}Ti^+$, $^{47}Ti^+$, $^{48}Ti^+$, $^{49}Ti^+$ and $^{50}Ti^+$ (line 1) and $^{46}Ti^+$, $^{51}V^+$ and $^{52}Cr^+$ (line 2) with integration times per cycle of 8.4 and 4.2 s, respectively. Each measurement comprised 40 scans with a magnet idle time between each peak jump of 3 s. Under the high-resolution mode argide interferences ($^{38}Ar^{12}C$, $^{36}Ar^{14}N$, and $^{40}Ar^{12}C$) could be resolved from the isotopes of interest ($^{50}Ti$ and $^{52}Cr$). Instrumental mass bias was corrected relative to $^{49}Ti/^{47}Ti = 0.749766$ (Leya et al., 2007) using an exponential law (e.g., Russell et al., 1978, Albarède and Beard 2004) as well as an equilibrium law (e.g., Wombacher and Rehkämper, 2003, Young and Galy, 2004). The isobaric interferences ($^{46}Ca$ on $^{46}Ti$, $^{48}Ca$ on $^{48}Ti$, $^{50}V$ and $^{50}Cr$ on $^{50}Ti$) were corrected following the procedure of Zhang et al. (2011), in which optimum isotope ratios of $^{46}Ca/^{44}Ca$, $^{48}Cr/^{44}Ca$, $^{50}V/^{51}V$ and $^{50}Cr/^{52}Cr$ were empirically estimated to eliminate apparent Ti isotope anomalies for a Ti standard solution doped with Ca, V or Cr. No significant level of $Zr^{2+}$ interference was observed during the sample measurements. The total procedural Ti blanks were less than 0.1 ng, while analyzed samples contained ~2 μg of Ti. The Ti isotope ratios of samples are expressed as the common epsilon (ε) notation relative deviation from the NIST SRM 3162a standard as $\varepsilon^{46,\ 48,\ \text{or}\ 50}Ti = 10^4 \times [(^{46,\ 48,\ \text{or}\ 50}Ti/^{47}Ti)_{sample}/(^{46,\ 48,\ \text{or}\ 50}Ti/^{47}Ti)_{NIST3162a} - 1]$. To evaluate the accuracy and precision of data obtained by the separation and instrumental protocols, we analyzed the international rock standard BCR-2 during the course of this study. We obtained $\varepsilon^{46}Ti = -0.17 \pm 0.30$, $\varepsilon^{48}Ti = -0.02 \pm 0.31$, and $\varepsilon^{50}Ti = -0.10 \pm 0.32$ (N = 8, 2 SD), which are consistent with the values reported in the previous study (Zhang et al., 2011).

# 3. RESULTS

## 3.1. Petrology

Northwest Africa 6704 is composed dominantly of large orthopyroxene grains, with smaller grains of Ni-rich olivine, feldspars (plagioclase and K-feldspar), chromite, NiFe-metal (awaruite), sulfides (heazlewoodite and pentlandite) and merrillite. The modal abundances of minerals were obtained for two thin sections (TS-6 and TS-7) from their phase maps obtained by X-ray intensity maps on the entire thin sections. The results are summarized in Table 2. The micro-CT images of individual minerals and the combined image of the major phases other than orthopyroxene are shown in Fig. 2a–e. As olivine and chromite have similar X-ray absorption coefficients, these minerals are shown together in Fig. 2b. Further, 3-D rotating or passing-through views of the mineral morphology can be seen in the Electronic annex Video files (EA. 2–8).

Orthopyroxene is identified by straight extinction under crossed nicols, EBSD patterns, and low CaO content. The size of orthopyroxene is mostly greater than a few mm and up to 1.7 cm in length. The grain size of orthopyroxene is highly variable on various scales and orthopyroxene grain larger than 0.5 cm is called as megacryst in this paper. Some of NWA 6704 fragments consist mostly of orthopyroxene megacrysts (TS-2–5, 7 and 9, termed as “coarse lithology”: Figs. 2a–e and 3a–c), whereas other fragments consist mostly of orthopyroxene with grain size 1 mm across on average and minor megacrysts (TS-1, 6 and 8, termed as “fine lithology”: Fig. 3d–f). Orthopyroxene megacrysts are either euhedral or subhedral. In the coarse lithology (Fig. 3a–c), the megacrysts are elongated parallel to the c-axes, and show a shape-preferred orientation (Fig. 4). In many places, the orthopyroxene megacrysts are in direct contact with each other without a clear interstitial part. Their boundaries are very irregular and indented on a grain-size scale, and thus the adjacent megacrysts are interlocked with each other. Orthopyroxene megacrysts contain abundant euhedral olivine and anhedral plagioclase, which tend to occur in the marginal zone of megacrysts. Some megacrysts also enclose curvilinear trains of irregularly-shaped micro-bubbles (Fig. 5a and b) as well as tiny oval-shaped inclusions of chromite (Fig. 5c). Raman spectroscopy demonstrates that the clear to pinkish bubbles are now empty. Both sorts of included objects are localized in the core and/or mantle of megacrysts, and in some places, are aligned parallel along the earlier growth surface.

Minor amounts of pigeonite occur as a rim surrounding some orthopyroxene megacrysts with thicknesses of up to a few hundred lm. The pigeonite and surrounded orthopyroxene share the same c-axis orientation. Augite ($Fs_{17}En_{45}$-$Wo_{39}$) occurs as exsolution lamellae in pigeonite. The lamellae have thickness up to ~0.1 μm with 1–2 μm spacing.

Plagioclase occurs mostly in orthopyroxene megacrysts as “inclusions” apparently isolated from each other in the coarse lithology, whereas it occurs along the grain boundaries or interstices of orthopyroxene and olivine grains in the fine lithology. Notably, plagioclase shares the same optical extinction positions over an area up to a few cm scale in both the coarse and fine lithologies. The EBSD analyses also indicate the identical lattice orientations of plagioclase over such area. Plagioclase often shows a cuspate morphology with extremely low dihedral angles of ≤40° against contacting two mafic crystals with distinct

crystallographic orientations irrespective of their assemblage (plagioclase-olivine-orthopyroxene, plagioclase-olivine-olivine, etc.). The dihedral angles are, however, greater than 60° on the scale of ~10 μm (Fig. 6–i). Some plagioclase domains enclosed in orthopyroxene megacrysts show rectangular morphology with both curvatures and straight interfaces with the host (Fig. 6–ii). Our EBSD analysis showed that such facets are parallel to c-axis of the adjacent orthopyroxene, and the shapes of plagioclase are consistent with [1 0 0], [0 1 0] and [0 0 1] axes of the orthopyroxene (Fig. 6). Moreover, some plagioclase domains have thin delicate maze-like morphology (Fig. 6–iii) extending into orthopyroxene megacrysts. These observations indicate that the apparently isolated grains of plagioclase are inter-connected with each other in three dimensions, which is recognizable in the obtained micro-CT image (Fig. 2d). Some plagioclase grains contain tightly clustered oval inclusions (Fig. 7), which tend to be aligned parallel to [1 0 0] axis of plagioclase, indicating that these inclusions were trapped during the crystallization of plagioclase. Twinning of plagioclase is vague and the wavy extinctions are not clearly observed. This indicates that NWA 6704 is unshocked to very weakly shocked, corresponding to shock stage S1 or S2 (Fritz et al., 2017).

Olivine occurs mostly as euhedral to subhedral grains with diameters from 50 μm to 1.7 mm and they are intimately associated with anhedral plagioclase. It shows sharp extinction under crossed-nicols, consistent with the low shock stage. Some olivine grains contain melt inclusions that are filled with glass containing bubbles and euhedral orthopyroxene skeletal crystals (Fig. 8a). In the coarse lithology, olivine is distributed in the outer parts of orthopyroxene megacrysts, rarely occurring along megacryst boundaries (Fig. 3c). In the fine lithology, the size of olivine is comparable to that of orthopyroxene, and the olivine is rather homogeneously distributed with clear avoidance of core regions of orthopyroxene megacrysts (Fig. 3f). In both the coarse and fine lithologies, olivine occasionally occurs as anhedral vermicular inclusions within orthopyroxene megacrysts (Fig. 8b). These vermicular olivine inclusions occur only in one place near the center of each orthopyroxene megacryst (e.g., red circles in Fig. 3a–e). The number of orthopyroxene megacrysts containing such vermicular olivine inclusions tends to be smaller for the coarse lithology: The thin sections of the fine lithology have more than five orthopyroxene megacrysts including vermicular olivine, whereas the thin sections of the coarse lithology have only a few of them. The EBSD analysis reveals that these inclusions have twisted crystallographic orientations.

Chromite is euhedral to subhedral and its size ranges from 30 to 300 μm in diameter. It is mostly present in the marginal part of orthopyroxene megacrysts together with plagioclase and olivine and it is absent in the core regions of orthopyroxene megacrysts. In fine-grained areas of the fine lithology, it occurs along grain boundary of olivine, mostly associated with plagioclase. Inclusions of chromite are also observed in olivine. Some chromite grains contain sub-rounded melt inclusions.

Awaruite is rounded in morphology and has a size ranging from 20 μm to 1 mm in diameter. In the coarse lithology, larger grains (~1 mm) are present with plagioclase and olivine in the margin of orthopyroxene megacrysts. Smaller grains (~20 μm) occur mainly as ovals or spherules, scattering among the texture. Inclusions of awaruite are observed in orthopyroxene, olivine, and plagioclase. Moreover, there are composite inclusions of Ni-Fe-

S minerals including awaruite and heazlewoodite with or without pentlandite (Fig. 8c). Some of the composite inclusions show rounded morphology, but others show facetted outline against the host orthopyroxene (Fig. 8c), which indicates that it was a single crystalline phase when incorporated in the host. Some of the larger awaruite grains are associated with orthopyroxene grains and the reaction rims of Fe and Ni-rich olivine are observed along the grain boundaries with thickness of 5 μm (Fig. 8d).

Merrillite has a rounded morphology and grain size ranging from 20 to 100 μm in diameter. It is associated with plagioclase or pigeonite, and sometimes occurs as oval inclusions in plagioclase.

The representative EPMA data (in wt.%) for individual phases are summarized in Table 3. The major element compositions of individual minerals are generally homogeneous among thin sections. Orthopyroxene is mostly homogeneous with the ferrosilite component (Fs = 100 × Fe/(Mg + Fe + Ca)) ranging from 40 to 42, enstatite component (En = 100 × Mg/(Mg + Fe + Ca)) from 55 to 57, and wollastonite component (Wo = 100 × Ca/(Mg + Fe + Ca)) from 3 to 4. The average value of Fe/Mn is 1.4. However, some orthopyroxene megacrysts have a chemically distinctive core characterized by low Ca and high Mg contents. The EPMA line profile (Fig. 9) illustrates that the core has relatively low Ca and Ti contents and high Mg# (the center: $Fs_{35}En_{64}Wo_{0.8}$) with gradual increases of Ca, and Ti and decrease of Mg towards the margin of Ca and Mg plateau (Ca = 0.02 mol%, Mg# = 60.5), which is rimmed by orthopyroxene with the “normal” Mg# (the shaded area in Fig. 9b–d; Ca = 0.02–0.03 mol%, Mg# = 57–60). The orthopyroxene rim is further surrounded by pigeonite having many exsolution of clinopyroxene.

Olivine has a slightly heterogeneous chemical composition ranging from 50 to 53 in fayalite content (Fa = 100 × Fe/(Mg + Fe)) with Fe/Mn = 1.1–2.1 and the average NiO = 0.9 wt.%. Vermicular olivine inclusions in the core regions of orthopyroxene megacrysts are richer in Fe ($Fa_{54–55}$) than “normal” olivine (Table 3).

Chromite has a Cr/(Cr + Al) ~ 0.94 and a notably high ferric content of ~2.2 wt.% of $Fe_2O_3$. Sub-rounded glass inclusions in chromite are rich in Fe, Ti and Mg as compared to glass inclusions in other phases (Table 3).

Ni-Fe metal is identified as awaruite with Ni contents ranging from 78 to 81 wt.% (Table 3). In Ni-Fe composite inclusions in orthopyroxene, awaruite has a chemical composition of $Fe_{20}Ni_{79}$, corresponding to relatively Ni-poor single awaruite grains, whereas heazlewoodite and pentlandite have compositions of $Fe_3Ni_{55}S_{42}$ and $Fe_{26}Ni_{24}S_{48}$, respectively.

Plagioclase is extremely Na-rich and classified as albite. It has slight heterogeneity with variation of albite content (Ab = 100 × Na/(Ca + Na+K)) from 91 to 93. It is also rich in orthoclase component (Or = 100 × K/(Ca + Na+ K)) ranging from 4 to 6, while the anorthite content (An = 100 × Ca/(Ca + Na+K)) varies from 2 to 3.

### 3.2. Geothermometry and geobarometry

The temperatures estimated by applying the two-pyroxene geothermometer of Lindsley and Andersen (1983) to 18 pairs of orthopyroxene and augite inverted from pigeonite range from

900 to 1200 °C, with an average of 1050 °C. Olivine-spinel Fe-Mg exchange geothermometry of Fabriés (1979) for neighboring spinel and olivine yields temperatures ranging from 850 to 970 °C with an average of 900 °C. The cooling rate of NWA 6704 can be constrained from the relationship between the calculated temperature of the average olivine composition and chromite core ($T^*$) and sizes ($\phi$ = ~35–260 μm in diameter) of respective chromite grains by applying geospeedometry established by Ozawa (1984). The $T^*$–$\phi$ diagram (Fig. 10) indicates a cooling rate of $10^{-4}$–$10^{-2}$ °C/h. Considering, however, that NWA 6704 is composed predominantly of orthopyroxene in which Mg-Fe diffusion is slower than in olivine, the actual cooling rate was slower than this estimate.

The coexistence of olivine, orthopyroxene, and spinel allows us to constrain the oxygen fugacity ($fO_2$) on the basis of the olivine-spinel oxygen geobarometry of Ballhaus et al. (1991). Using the temperature estimated from the olivine-spinel Fe-Mg exchange geothermometer for each chromite grain, the $fO_2$ is constrained to be 2.6 log units below the fayalite-magnetite-quartz buffer (FMQ −2.6). The result is consistent with the presence of Ni-rich metal (78–81 wt.% Ni) and ferric content in chromite (2.23 wt.% $Fe_2O_3$).

### 3.3. Major and trace elements

The measured whole rock and mineral compositions of NWA 6704 measured by solution-based ICP-MS are summarized in Table 4. The bulk major element compositions estimated using the modal mineral abundances obtained from the phase maps (Table 2) and mineral chemical compositions (Table 3) are also listed in the table. The XRF major element analysis of fragment #5 yielded substantially 6% lower $SiO_2$ and 4% higher FeO contents than the estimates on fragment #4 using the modal mineral abundance and mineral compositions, indicating chemical heterogeneity among the fragments. The Si/Mg ratio in the both fragments is distinctly higher than that in CI chondrites (Si/Mg ~ 1.9–2.2 × CI), whereas relative abundances of Na, Ni, Fe, Mn, K and Ca to Mg are similar to or slightly lower than those in CI chondrites (~0.8–1.0 × CI). In Fig. 11, the whole rock major and trace element abundances of NWA 6704, normalized to CI chondrite abundances (Palme and O'Neill, 2014), are plotted against the order of decreasing incompatibility to orthopyroxene (Kennedy et al., 1993; Bédard, 2007; Laubier et al., 2014) (Fig. 11a) and the 50% condensation temperature for a solar composition gas at $10^{-4}$ bar (Tc, Lodders, 2003) (Fig. 11b). The plots show that, relative to CI chondrite, NWA 6704 is depleted in elements having Tc of <900 K irrespective of lithophile, siderophile, or chalcophile (Fig. 11b), whereas there is no systematic change in the relative elemental abundances with the incompatibility (Fig. 11a). Among the two whole rock fractions analyzed for trace elements, fragment #3 has markedly higher abundances of Sr and Ba than fragment #6. Considering that these elements are sensitive indicators of terrestrial weathering (Barrat et al., 2003), the data suggest that fragment #3 is more affected by terrestrial weathering. Both of the two fragments show moderate depletion in heavy REE abundances as compared to CI chondrite (0.5 × CI) with only slightly light REE depleted to enriched patterns ($[La/Yb]_N$ = 0.63–2.1, [Eu/Eu*] = 0.84–1.09) (Fig. 12). The present data for NWA 6704 and NWA 6693 are generally consistent with those obtained for NWA 6693 by Warren et al. (2013), except for Cr, some REE, Ni, V, and Co. The differences may be partly due to the uneven distribution of minor phases such as Ni-Fe-metal, phosphate, and chromite between samples.

### 3.4. Highly siderophile elements and Re–Os isotopes

The HSE abundances and $^{187}Re$–$^{187}Os$ systematics for NWA 6704 are presented in Table 5. Highly siderophile element abundances, normalized to CI chondrite abundances (Orgueil; Horan et al., 2003) are shown in Fig. 13. The milligram-sized bulk fragments have broadly chondritic HSE abundances, ranging from ~0.2 × to ~5 × CI abundances of Ir. The metal fraction has much higher HSE abundances, with ~48 × CI Ir. By contrast, the silicate fraction has much lower HSE abundances than bulk fractions, with ~0.05 × CI Ir. The relative abundances of all fractions are only slightly fractionated from CI chondrite relative abundances. CI-normalized Re/Ir, Os/Ir, Ru/Ir, Pt/Ir, and Pd/Ir range from 0.7–1.7, 0.7–1.4, 0.8–1.7, 1.0–1.4, and 0.7–2.2, respectively. To estimate NWA 6704 HSE abundances at the whole-rock scale, the HSE abundances of the milligram-sized bulk fragments were averaged, weighted by mass (Fig. 13). Although the HSE abundances of a calculated whole rock composition are similar to bulk chondrites, on a finer scale there are HSE fractionations and large variations in the absolute HSE abundances among milligram-sized bulk fragments.

The $^{187}Re$–$^{187}Os$ systematics are shown in Fig. 14. The milligram-sized bulk fragments have $^{187}Os/^{188}Os$ ranging from 0.121 to 0.147, while those ratios in metal and silicate fractions are within the range. The $^{187}Os/^{188}Os$ in the bulk and metal fractions are correlated well with Re/Os but not with 1/Os (Fig. 14a and b), indicating that the regression line in Fig. 14a represents not a mixing line but an isochron. The isochron regression using ISOPLOT (Ludwig, 2001) defines an age of 4576 ± 250 Ma, indicating early Solar System closure of the isotope system. By contrast, the silicate fraction plots below this isochron (Fig. 14a). The $^{187}Re$–$^{187}Os$ systematics of these samples can be expressed in $\Delta_{Os}$ units (where $\Delta_{Os}$ is the deviation in parts per 10,000, from a primordial 4568 Ma reference isochron, using parameters from Becker et al. (2001) and Archer et al. (2014) ($\Delta Os = 10^4 \times [^{187}Os/^{188}Ossample - [0.09517 + 0.07908 \times {}^{187}Re/^{188}Os_{sample}]]$). The $\Delta_{Os}$ of bulk samples and metal range from +0.8 to +6.8, whereas the silicate sample has a $\Delta_{Os}$ value of −24 ± 10 (Table 5; Fig. 14c). The larger error bars for the silicate are the result of low Re and Os abundances, and consequently, larger blank corrections.

### 3.5. Oxygen and Ti isotopes

The results of O isotope analyses of NWA 6704 are summarized in Table 6, together with those of a different fragment of NWA 6704 (Irving et al., 2011) and paired NWA 6693 (Warren et al., 2013). The five fractions analyzed in this study yielded slightly variable $\delta^{18}O$ and $\delta^{17}O$ values but identical $\Delta^{17}O$ values within analytical uncertainty. Moreover, the $\delta^{18}O$ and $\delta^{17}O$ values are clearly distinct from the previously reported values for NWA 6704 (Irving et al., 2011), while the $\Delta^{17}O$ values are consistent with those of Irving et al. (2011). The variations in the $\delta^{18}O$ and $\delta^{17}O$ values can be attributed to the difference in mineral abundance among the analyzed fractions. Our results yield an average $\Delta^{17}O$ value of –1.052 ± 0.004 (2 SD), which is similar to the $\Delta^{17}O$ value of –1.08 obtained from paired NWA 6693 (Warren et al., 2013).

The Ti isotope ratios normalized using the exponential law are presented in Table 7, whereas those using the equilibrium law are reported in Table EA-9. There are no resolvable differences between $\varepsilon^{46,\ 48,\ or\ 50}Ti$ values obtained with the exponential and equilibrium

laws, and the former will be used for the following discussion. The two analyzed chromite fractions yielded identical results. The average $\varepsilon^{46}$Ti and $\varepsilon^{48}$Ti values are 0.06 ± 0.39 and 0.21 ± 0.54 (2 SD), which are indistinguishable from the results of the terrestrial basalt BCR-2. By contrast, the average $\varepsilon^{50}$Ti value of 2.28 ± 0.23 (2 SD) is markedly higher than that of the terrestrial rock. The Ca/Ti, V/Ti and Cr/Ti ratios in the measured sample fractions are $2.0 \times 10^{-3}$, $10^{-5}$, and $10^{-5}$, respectively. There is no correlation between $\varepsilon^{50}$Ti and V/Ti nor Cr/Ti, indicating that the observed $^{50}$Ti excess in NWA 6704 is not an analytical artifact of the interferences of $^{50}$Cr and $^{50}$V. These results are consistent with those obtained for a whole rock fraction of NWA 6704 (Sanborn et al., 2019). Furthermore, the $\varepsilon^{50}$Ti and $\varepsilon^{46}$Ti values are plotted on the correlation line proposed for Solar System objects by Trinquier et al. (2009) ($\varepsilon^{50}\text{Ti} = (5.48 \pm 0.27) \times \varepsilon^{46}\text{Ti} - (0.04 \pm 0.20)$) within analytical uncertainty.

## 4. DISCUSSION

### 4.1. Crystallization process of NWA 6704

The overall texture of NWA 6704 is characterized by interlocking aggregate of orthopyroxene megacrysts with finer euhedral-subhedral olivine and anhedral plagioclase. The crystallographic consistency of the apparently isolated plagioclase domains indicates that the apparent “inclusions” are inter-connected in three dimensions, and thus orthopyroxene megacryst and plagioclase are interlocked. The dihedral angles of plagioclase against contacting two mafic crystals are very low ($\theta \leq 40°$), but the tips of plagioclase are rounded on the scale of ~10 μm (Fig. 6–i), implying that plagioclase crystallized from melt filling interstices of mafic minerals and its morphology was frozen at the stage approaching the textural equilibrium characterized by the median angle populations of 100°–130° for granulite-grade rocks (Kretz, 1966; Vernon, 1968, 1970). In addition to these dihedral angle features, the coexistence of curvatures (or cuspate) and straight interfaces (Fig. 6–ii) is consistent with the growth of orthopyroxene narrowing melt filled spaces before the crystallization of plagioclase. Further, such facets are parallel to the c-axis of orthopyroxene (Fig. 4), indicating that the outline of plagioclase is controlled by the rational crystal facets of orthopyroxene megacrysts. These observations strongly suggest that orthopyroxene megacrysts of NWA 6704 originally had “hollow” structures, and that plagioclase filled the space of a well-connected, complex network of pores in the megacrysts.

Minor phases in NWA 6704 include pigeonite, chromite, metal, sulfides and merrillite. Pigeonite occurs as rims on some orthopyroxene megacrysts, whereas the other minor phases are intimately associated with olivine and plagioclase. These observations indicate that the orthopyroxene started to crystallize in the melt before the other phases. Moreover, the occurrence of chromite and awaruite as inclusions in olivine indicates that they crystallized earlier than olivine. On the other hand, merrillite occurs in the margin of olivine as well as orthopyroxene. Thus, the following crystallization sequence is inferred: orthopyroxene (pigeonite) → awaruite, chromite → olivine → merrillite → plagioclase. Besides, the compositional variations observed in some orthopyroxene megacrysts containing Mg-rich cores (Fig. 9) indicate that the mantle characterized by the Ca and Mg plateaus grew slightly before the crystallization of “normal” orthopyroxene, which was followed by the overgrowth of pigeonite. The chemically distinct core is considered to

represent a relict grain from the precursor, which must have existed before the crystallization of the megacryst. The gradual compositional change is attributed to diffusion between the relict core and the host magma before the major crystallization stage of orthopyroxene. The vermicular olivine may also be inherited from the precursor, given that they always occur in cores of orthopyroxene megacrysts and have distinct chemical and crystallographic features from the normal olivine (Table 3).

Our EBSD mapping demonstrates that elongation of orthopyroxene megacrysts is along c-axis (Fig. 4). Such extension of single crystals in preferred growth orientations generally forms dendrites, a crystal having a branching structure with uniform lattice and optical properties throughout (Cody and Cody, 1995). Hence, the organized subdivision into sub-parallel units of megacrysts suggests their crystallization by dendritic growth and ripening, rather than by a complex combination of nucleation or crystal aggregation (Welsch et al., 2012). Such dendritic structure of each orthopyroxene megacryst is partly recognizable in the micro-CT images (Fig. 2a and EA-7).

Branching, dendritic crystals generally form under extreme super-saturation conditions (Lofgren, 1980; Vetere et al., 2015), suggesting that the initial cooling rate of NWA 6704 was very rapid. Crystal morphology as a function of cooling rate was investigated for various melts by dynamic crystallization experiments (e.g., Lofgren, 1980). The results for basaltic compositions showed that the typical crystal shape is euhedral-equant and slightly skeletal or blocky at <2 °C/h, elongate and skeletal to even more acicular at 2–10 °C/h, dendritic to spherulitic at >10 ° C/h, and a feathery texture as observed in “spinifex-textured rock” (Fleet and MacRae, 1975) at >50 °C/h. Vetere et al. (2015) confirmed that elongated dendrites can form even by heterogeneous crystallization at cooling rates of 7–60 °C/h from the starting temperature of 1300 °C, whereas crystallization is suddenly suppressed at >1800 °C/h from the same starting temperature, leaving glassy products. These experiments were mostly on clinopyroxene, olivine, and plagioclase, which could show morphological behaviors distinct from orthopyroxene. Nevertheless, skeletal or dendritic orthopyroxene has been reported from rapidly solidified terrestrial rocks, such as komatiite lavas (Arndt and Fleet 1979) and orbicular diorite intrusions (Durant and Fowler, 2002), suggesting that orthopyroxene dendrite could form essentially in the same manner as clinopyroxene. Thus, we infer that the initial cooling rate of NWA 6704 was most likely about $1–10^2$ °C/h (dendrite formation conditions) and not higher than $10^3$ °C/h (glass formation conditions).

The grain sizes of the NWA 6704 orthopyroxenes (0.4–1.7 cm) are significantly larger than dendritic crystals observed in eucrites or lunar and Martian basalts (μm to ~mm; Barrat et al., 2003; Walton and Herd, 2007; Hewins and Zanda, 2012). Such coarse dendritic crystals would be formed when very few nuclei exist in the superheated parental melt at the onset of cooling, so as to suppress homogeneous nucleation (Walton and Herd, 2007). Remarkably, a thin section of the fine lithology tends to contain more orthopyroxene grains with Mg-rich cores and vermicular olivine inclusions that are considered to be inherited components from the precursor (Fig. 8b and 9). The relationship may reflect that these cores acted as nuclei for the dendritic growth of orthopyroxene giving rise to megacryst formation when such nuclei are limited in number.

In contrast to the initial very high cooling rate to produce the dendritic texture for orthopyroxene, the olivinespinel geospeedometry indicates a significantly slower cooling rate of $<10^{-4}$–$10^{-2}$ °C/h at 850–970 °C (Fig. 10). A similar cooling rate of $2.0 \times 10^{-2}$ °C/h at a temperature interval between 1100 and 950 °C is estimated from the thickness and wavelength of some augite exsolution lamellae that are similar to those observed in the Zagami martian meteorite (Brearley, 1991; Takagi et al., 2014). These results indicate that the cooling rate significantly decreased below a temperature of ~1100 °C during the cooling of NWA 6704.

On the basis of the textural and mineral chemical data and the above considerations, the following crystallization processes are inferred for NWA 6704: (1) the parental magma was initially dominated by melt with a few grains of relict Mg-rich orthopyroxene and vermicular olivinebearing orthopyroxene, (2) orthopyroxene rapidly crystallized under highly super-saturation conditions, mostly on the preexisting seeds, which suppressed homogeneous nucleation and resulted in the formation of orthopyroxene megacrysts with dendritic and branching morphology, (3) as the temperature fell with decreasing cooling rate, the dendritic growth of orthopyroxene ceased and thickening of the branches proceeded with crystallization of awaruite and chromite followed by olivine and merrillite, narrowing the pore space between the orthopyroxene branches, (4) plagioclase started crystallization with limited numbers of nuclei when a interstitial residual melt was still well-connected, and eventually it completely filled the pore space.

The initial state of the crystallization can be further explored from the diffusional zoning developed around the relict Mg-rich core of orthopyroxene megacryst. Applying the average $Fe^{2+}$-Mg interdiffusion coefficient along the c and b axis directions of orthopyroxene of Ganguly and Tazzoli (1994), the diffusional profile indicates that the time scale of heating and cooling was on the order of $<10^2$ s. Such instantaneous melting is consistent with the presence of vermicular olivine inclusions. Reaction experiments between natural olivine crystals ($Fo_{91}$, $Fo_{39}$, and $Fo_{31}$) and $SiO_2$-rich melt at high temperatures (1100–1320 °C) showed that vermicular olivine can form via its partial dissolution under the conditions where the olivine has an Fe content higher than the equilibrium Fe content of olivine with the melt and when the duration of heating is too short ($<10^2$ h at >1300 °C) to dissolve the Fe-rich olivine out (Tsuchiyama, 1986).

Most of the petrologic and mineral chemical features of NWA 6704 described above are consistent with those reported for paired NWA 6693, such as the intact igneous texture with the lack of shock metamorphic features, optical continuity of plagioclase over large areas, micro-inclusion alignments in plagioclase, and Ni-rich olivine, metal and sulfide compositions, even though an olivine-rich clast reported for NWA 6693 (Warren et al., 2013) has not been found in NWA 6704. Nevertheless, the inferred crystallization process is inconsistent with previously proposed cumulate origin for NWA 6693/6926 by Warren et al. (2013), who interpreted that NWA 6693 underwent an intense shock after its formation as a cumulate, causing selective melting of plagioclase and infiltration of the melt to account for the optical continuity of plagioclase. However, the dendtritic structure of orthopyroxene megacrysts and the presence of glass- and skeletal orthopyroxene-bearing inclusions in olivine (Fig. 8a) provide strong evidence for rapid cooling during crystallization of the mafic

minerals. In addition, as discussed below, the rapid initial crystallization rather than cumulate origin can be more readily reconciled with the lack of chemical evidence for significant magmatic fractionation.

### 4.2. Highly siderophile element systematics of NWA 6704

Although the $^{187}Re$–$^{187}Os$ system cannot be used for precise dating of NWA 6704 formation because of the limited variation in Re/Os, it is useful for placing constraints on the occurrence and timing of secondary processes that may have affected the HSE in NWA 6704 fractions. The $^{187}Re$–$^{187}Os$ systematics of NWA 6704 bulk and metal fractions are generally consistent with system closure since formation, given that they fall on or near a primordial isochron (Fig. 14a). The deviation of the silicate fraction from a primordial isochron most likely indicates that a minor amount of Re has been added (Fig. 14c). Prior studies have noted similar disturbances of the Re–Os systems in some samples from Northwest Africa (Brandon et al., 2012). Despite the minor disturbance, the HSE abundances of the silicate sample were not evidently affected by secondary processes by more than a few percent.

The relative and absolute HSE abundances of bulk fragments are broadly chondritic, but variable among individual fragments. The variation in HSE abundances indicates that HSE carriers are heterogeneously distributed on a milligram scale in NWA 6704. The heterogeneity most likely reflects a nugget effect of HSE-rich carriers, as argued by Warren et al. (2013) for paired NWA 6693. Further, some modest Re/Os variations among different bulk fragments may be partly attributed to Re/Os fractionation caused by changing redox states, as Re has the highest oxidation potential among the HSEs. Indeed, the occurrence of Feand Ni-rich olivine grains observed along the boundaries between large awaruite and orthopyroxene grains (Fig. 8d) suggests olivine formation via oxidation reaction of awaruite consuming orthopyroxene during cooling.

Warren et al. (2013) reported depletions in the abundances of S and chalcophile elements relative to bulk CI chondrites in paired NWA 6693. In addition to being siderophile, the HSE, and especially Pd, are also chalcophile. Sulfides in iron meteorites can have Pd abundances that are ~10% of the Pd abundances of coexisting Fe, Ni-rich metal (Carlson and Hauri, 2001). Therefore, sulfide loss may result in Pd depletions and HSE fractionations if sulfides act as a major HSE carrier. However, bulk fragments of NWA 6704 do not have Pd depletions. Therefore, despite the loss of S and chalcophile elements (and possibly sulfide phases), Pd behaved coherently with the other HSE and remained almost wholly retained in the metal. Evidently, under the formation conditions of NWA 6704, Pd behavior was far more siderophile than chalcophile.

Igneous processes should have equilibrated the HSE among metals and silicates. However, the apparent NWA 6704 metal/silicate concentration ratio for Ir is ~960. Although metal-silicate partition coefficients tend to decrease with increasing pressure and temperature for at least some HSE (e.g., Mann et al., 2012), even under P-T conditions appropriate for the terrestrial lower mantle, partition coefficients for Ir do not decrease below ~$10^4$. Thus, the HSE abundances of the measured NWA 6704 silicate fraction either reflect disequilibrium or the presence of some small fraction of HSE- rich metal or sulfide. Mixing calculations indicate that the presence of only 0.2% of the measured metal in a virtually HSE-free silicate

fraction can broadly account for the HSE abundances in the silicate fraction. However, the relative HSE abundances of the metal and silicate fraction are not identical (Fig. 13). Therefore, metal or sulfide present in the silicate fraction must have relative HSE abundances that differ from the measured metal fraction. This may reflect restricted addition of exogenous HSE-enriched, possibly impactor materials during or subsequent to magmatic crystallization, as observed for some basaltic achondrites (Riches et al., 2012). Note, however, that such contamination should have trivial effect on the HSE systematics of bulk and metal fractions because of their higher abundances. Indeed, their $^{187}Re$–$^{187}Os$ systematics define a primordial isochron rather than a mixing line (Fig. 14a and b).

### 4.3. Constraints on parent body processes

Multiple processes, including core formation, silicate differentiation, and degassing, can give rise to chemical variations among different parts of planetary bodies. Immediately following core formation, the HSE concentrations of the silicate portions of planetary bodies were most likely highly depleted and fractionated, relative to chondrites (e.g., Capobianco et al., 1993) because the HSE have high ($>10^4$–$10^6$ under low pressure conditions) and variable metal-silicate partition coefficients (e.g., Kimura et al., 1974; Newsom, 1990; O'Neill et al., 1995; Borisov and Palme, 1995; Fortenfant et al., 2003). In addition, the HSE are typically fractionated during silicate differentiation because of their diverse compatibilities in silicate systems (e.g., Barnes et al., 1985; Walker et al., 1999; Puchtel et al., 2004, 2007; Day et al., 2010). The absolute and relative HSE abundances of a calculated whole rock, which were calculated from the four bulk fragments, are broadly chondritic (Fig. 13). Except for Pd, the HSE abundances of the estimated whole rock composition are within 2r of carbonaceous, ordinary, enstatite, and Rumuruti-like chondrites (Fig. 15a), and one of the bulk fragments has HSE abundances that are within 2σ of ordinary chondrites for all HSE, including Pd. The HSE of NWA 6704 are also less fractionated than primitive achondrites, including ureilites, brachinites, brachinite-like achondrites, and GRA 06129 (Fig. 15b). Further, Warren et al. (2013) reported that the relative and absolute abundances of siderophile elements (including Co, Ni, Ir, Os, and Au) and non-volatile lithophile elements of paired NWA 6693 are only minimally fractionated relative to bulk chondrites. The nearly chondritic absolute and relatively unfractionated HSE abundances of NWA 6704 and NWA 6693 indicate that their precursor rocks most likely had chondritic absolute and relative HSE abundances, and that they crystallized from a melt that underwent only minor metal and sulfide fractionation. This, in turn, suggests that a parent body had not segregated metal or sulfide on a global scale to form a core by the time the samples formed.

The significance of the parent body differentiation can be further constrained from other geochemical systematics of NWA 6704. Silicate differentiation processes including crystal accumulation should cause significant fractionation between elements having highly different compatibilities in silicate systems. The CI chondrite-normalized REE pattern of NWA 6704 is compared with those of NWA 6693 and primitive achondrites in Fig. 12. The absolute abundances of REE in NWA 6704 and NWA 6693 are slightly sub-chondritic (0.4–0.7 × CI), which led some to argue its cumulate origin (Jambon et al., 2012; Warren et al., 2013). However, the only weakly fractionated REE patterns of NWA 6704 and NWA 6693 (Fig. 12), together with the lack of systematic depletion of highly incompatible lithophile

and siderophile elements (Fig. 11b and 13), require that neither the parental magma nor precursor underwent significant silicate differentiation.

A plot of Fe/Mn ratio vs. Fe/Mg ratio (Fig. 16) can be used to evaluate chemical fractionation during planetary processes, because (1) silicate differentiation is accompanied by variation in Fe/Mg ratio with minor Fe/Mn fractionation, (2) metal-silicate segregation causes correlated changes in Fe/Mn and Fe/Mg ratios, and (3) volatility-controlled differentiation can lead to more variation in Fe/Mn ratio than in Fe/Mg ratio (Goodrich and Delaney, 2000). Like primitive achondrites, NWA 6704 yields a Mn/Mg ratio (~1.06 × CI) within the range of chondritic ratios. As compared to primitive achondrites including lodranites and winonaites/IAB (~0.73 × CI and ~0.65 × CI, respectively), NWA 6704 has Fe/Mn and Fe/Mg ratios (Fe/Mg ~ 1.18 × CI; Fe/Mn ~ 1.11 × CI) similar to those of carbonaceous chondrites, which is consistent with the restricted silicate differentiation and metal-silicate segregation.

NWA 6704 is severely depleted in elements having Tc of <900 K, relative to the reference CI chondrite (Fig. 11b). Such depletion is recognizable for NWA 6693, but the degrees of the depletion are remarkably different between the two meteorites especially for Rb, Pb, and Te (Table 4). Further, a whole rock sample of NWA 6693 used for Rb–Sr dating has a nearly chondritic Rb abundance of 3.2 μg/g, which is one order of magnitude higher than that of NWA 6704 (Amelin et al., 2019). As a result of the Rb abundance variation, mineral separates of NWA 6704 and NWA 6693 yielded clearly distinct $^{87}Rb/^{86}Sr$ and $^{87}Sr/^{86}Sr$ ratios, but the Rb–Sr isotope data define a single isochron with an age of 4.54 ± 0.03 Ga, which is consistent with the Pb–Pb and Al–Mg ages (Amelin et al., 2019; Sanborn et al., 2019). This indicates that the observed Rb variation was established at or around the time of crystallization, implying that the depletion of the highly volatile element with variable degrees resulted from a high-temperature magmatic event forming NWA 6704 and NWA 6693.

Limited chemical fractionation among elements with $T_C$ > 900 K indicates that the effects of planetary differentiation processes must have been restricted for NWA 6704 and NWA 6693 compared to primitive achondrites characterized by more fractionated chemical compositions. The large-scale distributions of HSE-rich carriers (primarily metal and sulfides) in NWA 6704 appear to have been largely unchanged during melting and crystallization. Transport of these carriers must have therefore been limited. Moreover, fractional melting in the precursor and crystal accumulation in the parental magma should have been insignificant. One possibility for the restricted differentiation despite melting and crystallization is that the NWA 6704 parent body was too small for gravitational separation of metals, sulfides or silicate minerals from melt. Alternatively, melting and crystallization may have happened on a timescale that was too short to allow segregation of these phases. The latter is compatible with the petrological observations suggesting instantaneous melting followed by rapid crystallization. Plausibly, a chondrite-like precursor to NWA 6704 was rapidly heated well above liquidus temperature such that the generated melt contained a limited number of relics from the precursor and retained the primitive chemical features except for the highly volatile elements with Tc of <900 K that were lost by degassing. This rapid heating was immediately followed by rapid cooling, which resulted in the formation of

dendritic orthopyroxene megacrysts and prevented silicate differentiation and metal/sulfide segregation. Such precipitous thermal phenomenon may be implemented by an impact event, even though no unambiguous mineralogical evidence for this proposal, such as the presence of high-pressure phases, is preserved in NWA 6704.

### 4.4. Constraints on the provenance of the parent body

The O isotope compositions of meteorites have long been used to investigate their parent bodies, since different meteorite groups and, by extension, different planets have distinct $\Delta^{17}O$ values, probably as a result of isotope-selective photo-dissociation of CO in the early solar nebula (Clayton, 2002; Yurimoto and Kuramoto, 2004; Lyons and Young, 2005). More recently, it has been shown that each meteorite group has distinctive mass independent isotope variations of heavier elements such as Ti, Cr, and Ni (Trinquier et al., 2007, 2009; Dauphas and Schauble, 2016, and references therein). In particular, carbonaceous chondrites have substantially higher values of $\varepsilon^{50}Ti$ and $\varepsilon^{54}Cr$ as compared to most differentiated meteorites and ordinary and enstatite chondrites. The carbonaceous chondrite parent bodies (C-type asteroids) are considered to have accreted in the outer solar system and then implanted into the main asteroid belt (Walsh et al., 2011). Thus, the isotope data are interpreted to reflect distinct isotope features between the inner and outer early solar nebula (Warren, 2011; Budde et al., 2016; Van Kooten et al., 2016; Kruijer et al., 2017). This potentially offers a new means of assessing the parent body provenance, even though the cause of the isotope variations is a matter of on-going debate (e.g., Trinquier et al., 2009; Dauphas et al., 2010; Qin et al., 2011). In Fig. 17, we compare the O–Ti–Cr isotope systematics of NWA 6704 and other planetary materials (the $\varepsilon^{54}Cr$ value of 1.69 ± 0.07 for NWA 6704 is from Sanborn et al., 2019). The comparison shows that NWA 6704 plots within the range of carbonaceous chondrites. This correspondence suggests that its parent body sampled the same reservoirs of O, Ti and Cr in the outer solar system as the carbonaceous chondrite parent bodies. If so, it is likely that the precursor of NWA 6704 was originally hydrous, but water was lost during the magmatic event together with the highly volatile elements such as Rb. The empty inclusions observed in the orthopyroxene megacrysts (Fig. 5a and b) may represent a vestige of trapped fluid that was derived from the hydrous precursor.

NWA 6704 shows further similarities to carbonaceous chondrites in $fO_2$ and refractory major element abundances. The $fO_2$ of NWA 6704 (FMQ −2.6) estimated from the olivine-spinel geobarometry is similar to those of CV chondrites and distinctly higher than those of ordinary and enstatite chondrites (Righter and Neff, 2007), suggesting its parent body accretion in a relatively oxidized environment. The Al/Mg and Ca/Mg ratios in NWA 6704 (Al/Mg ~ 1.27 × CI; Ca/Mg ~ 1.06 × CI) are within the range of carbonaceous chondrite values (Al/Mg 0.98–1.37 × CI; Ca/Mg 0.97–1.38 × CI), while those ratios are distinctly lower in non-carbonaceous chondrites (Al/Mg 0.84–0.93 × CI; Ca/Mg 0.75–0.94 × CI) that have lower abundances of refractory Ca-Al-rich inclusions (CAIs) in non-carbonaceous chondrites (e.g., Palme, 2000; Rubin, 2011) (Fig. 18).

On the other hand, NWA 6704 is clearly distinct from both carbonaceous and non-carbonaceous chondrites in its high Si/Mg (~1.85 × CI; chondrites and primitive achondrites

0.62–1.40 × CI). Such elevated Si/Mg ratio is observed also in NWA 6693 (Warren et al., 2013) and results in their higher modal ratios of low-Ca pyroxene to olivine than those in carbonaceous chondrites. The high Si/Mg ratio in NWA 6704 cannot be attributed to igneous differentiation on its parent body, because the nearly chondritic HSE and only weakly fractionated REE patterns preclude significant magmatic fractionation (previous section). Aqueous alteration processes are incapable of fractionating Si from Mg without a remarkable change of Fe/Mg ratio (Tomeoka and Buseck, 1985; McSween, 1987) that is not observed in NWA 6704. It is difficult to account for the increased Si/Mg ratio by volatilization processes on the parent body, given the rather chondritic Na/Mg and K/Mg ratios in NWA 6704 and NWA 6693 (Fig. 18) despite more volatile features of Na and K relative to Si. Instead, the Si enrichment in NWA 6704 may result from cosmo-chemical fractionation in the solar nebula that is thought to be responsible for Si/Mg variations among different chondrite groups (Larimer, 1979).

It has long been known that carbonaceous and non-carbonaceous chondrites define distinct trends in a Mg/Si vs. Al/Si diagram (Fig. 19) (Jagoutz et al., 1979; Larimer, 1979; Alexander, 2005): there are little Mg/Si variations but significant Al/Si variations for carbonaceous chondrites, whereas correlated variations between Mg/Si and Al/Si ratios are observed for non-carbonaceous chondrites. On the basis of predicted condensation sequence for the cooling solar nebula, the cosmochemical trend for carbonaceous chondrites has been considered to reflect the addition of the earliest condensates to the solar (CI) composition, whereas that for non-carbonaceous chondrites has been explained by the removal of forsterite and earlier condensates (Larimer, 1979). The nebular fractionation of forsterite is consistent with a more recently recognized correlation between the Mg/Si ratios and Si isotopic compositions of different meteorite groups (Fitoussi et al., 2009; Dauphas et al., 2015).

If the significantly lower Mg/Si ratio in NWA 6704 (Mg/Si ~ 0.52 × CI) is due to the nebular fractionation, then the NWA 6704 parent body likely formed in a region of the protoplanetary disk where the forsterite component was significantly depleted as compared to the accretion regions of any known chondrites. At the same time, the remarkable deviation of NWA 6704 from the noncarbonaceous chondrite trend (Fig. 19) suggests that the most refractory component was relatively enriched in the region. Given that CAIs and refractory presolar materials exhibit high $\varepsilon^{50}$Ti and $\varepsilon^{54}$Cr values (e.g., Choi et al., 1998; Trinquier et al., 2009; Qin et al., 2011; Kööp et al., 2016), the refractory component enrichment in NWA 6704 can account for its carbonaceous chondrite-like Ti and Cr isotopic compositions despite of its non-chondritic Mg/Si ratio.

## 5. SYNTHESIS AND IMPLICATIONS

The unique achondrite NWA 6704 consists of orthopyroxene megacrysts with finer interstitial crystals of olivine, chromite, awaruite, sulfides, plagioclase and merrillite. The petrology, morphology and mineral chemistry collectively indicate the following crystallization sequence for NWA 6704: (1) melt-dominant state with a few grains of relict Mg-rich orthopyroxene and vermicular olivine-bearing orthopyroxene, (2) following rapid growth of orthopyroxene mostly on the preexisting seeds under high super-saturation

conditions, which suppressed homogeneous nucleation and resulted in the formation of orthopyroxene megacrysts (up to ~1.7 cm) with dendritic and branching morphology, (3) as the temperature fell, dendritic growth of orthopyroxene ceased and thickening of branches proceeded with crystallization of awaruite and chromite followed by olivine and merrillite in the pore space between the orthopyroxene branches, and (4) finally plagioclase crystallized with limited numbers of nuclei and filled the well-connected pore space, resulting in the interlocking between plagioclase and othropyroxene megacrysts. The diffusional zoning profile in a high Mg# pyroxene core, together with the presence of vermicular olivine inclusions, indicates that the initial melt-dominant state was instantaneous. The dendritic textures of orthopyroxene also indicate its rapid crystallization under super-cooling (1–$10^2$ °C/h) conditions. By contrast, the olivine–spinel geospeedometry records the notable decrease in cooling rate at a later stage of crystallization (<$10^{-4}$–$10^{-2}$ °C/h at below ~1100 °C).

The Re–Os isochron age of 4576 ± 250 Ma, defined by the bulk and metal fractions, suggests system closure since crystallization. The roughly chondritic HSE abundances of the bulk fragments with only weakly fractionated HSE and REE patterns require that the parental melt and precursor had undergone neither significant segregation of metals, sulfides, nor silicate minerals. Furthermore, the variable degrees of depletion in elements having Tc of <900 K relative to chondrites suggest volatilization of the elements during the magmatism to form NWA 6704. The limited chemical fractionations among moderately and highly refractory elements during the igneous event can be attributed to the short-time scale of the melting of the precursor and following crystallization. The precipitous thermal event might occur as a result of an impact event, even though no diagnostic impact features are observed in the mineralogy of NWA 6704. Such impact melting has been previously inferred for the origin of acapulcoites, lodranites, and ureilites (Rubin, 2007; Warren and Rubin, 2010), while others have proposed that the internal radioactive decay of $^{26}$Al was the heat source for melting and metamorphism of these meteorites (e.g., McCoy et al., 1996; Touboul et al., 2009; Keil and McCoy, in press). The consistent U–Pb (4562.76 + 0.22/−0.30 Ma: Amelin et al., 2019), Al–Mg (4563.13 ± 0.27 Ma, Sanborn et al., 2019) and Mn–Cr ages (4562.17 ± 0.76 Ma, Sanborn et al., 2019) of NWA 6704 indicate that the parent body accreted within ~4 Ma after CAI formation. It is, therefore, most likely that the parent body was internally heated by $^{26}$Al decay. However, heating solely by the internal radioactive decay would not cause rapid melting well above liquidus temperature as inferred for NWA 6704. We envision that an impact event on the radioactively heated, but not differentiated parent body induced a regional instantaneous melting up to a super-liquidus temperature immediately followed by rapid cooling. As a result, coarse orthopyroxene dendrites crystallized from the generated melt having a chondritic composition on the surface. The decrease of cooling rate in the late stage of the crystallization may reflect its burial under hot debris piled up within an ejecta blanket. Assuming that the cooling proceeded essentially by thermal conduction with a thermal diffusivity of $10^{-7}$ $m^2$/s (Horai and Winkler, 1974), the burial depth is estimated to be on the order of ~$10^2$ m.

The O and Ti isotope compositions of NWA 6704 are similar to those of carbonaceous chondrites and distinct from those of non-carbonaceous chondrites. The Cr isotope data provide a consistent view of the isotopic similarity to carbonaceous chondrites (Sanborn et

al., 2019). Further similarities between NWA 6704 and carbonaceous chondrites are observed in $fO_2$ and refractory major element abundances such as Ca/Mg and Al/Mg ratios. However, NWA 6704 has a Mg/Si ratio significantly lower than observed in carbonaceous chondrites and non-carbonaceous chondrite trend. These findings imply that the NWA 6704 parent body formed under oxidized conditions in an outer region of the solar system where nebular fractionation of forsterite and earlier condensates proceeded efficiently, followed by implantation of a refractory component having elevated $\varepsilon^{50}$Ti and $\varepsilon^{54}$Cr values.

## Supplementary Material

Refer to Web version on PubMed Central for supplementary material.

## ACKNOWLEDGEMENTS

We are grateful to A. Okubo, K. Ichimura, H. Yoshida, O. Sasaki, T. Tsuihiji, K. Yoshizawa, S. Kuehner, and R. Conrey for analytical support and Y. Amelin, V. A. Fernandes, M. Kimura, T. Mikouchi, T. Noguchi, and Y. Takagi for discussions. We also would like to thank Greg Hupé and John Kashuba for kindly providing us the images of NWA 6704, and Jean-Alix Barrat for providing us constructive comments and the whole rock chemistry data. This work is funded by Japan Society for the Promotion of Science (Core-to-Core Program “International Network of Planetary Sciences”; Grants #16J04429 to YH; Grant #25707042 and #26220713 to TI) and NASA (Cosmochemistry grant NNX13AF83G to RJW, Emerging Worlds grant NNX16AD34D to QZY).

## REFERENCES

Albarède F and Beard B (2004) Analytical methods for nontraditional isotopes. Rev. Mineral. Geochem 55, 113–152.

Alexander CMD (2005) Re-examining the role of chondrules in producing the elemental fractionations in chondrites. Meteoritics Planet. Sci 40, 943–965.

Amelin Y, Koefoed P, Iizuka T, Fernandes VA, Huyskens MH, Yin Q-Z and Irving AJ (2019) U–Pb age and extant radionuclide systematics of the ungrouped achondrites Northwest Africa 6704 and Northwest Africa 6693. Geochim. Cosmochim. Acta 245, 628–642.

Anders E and Goles GC (1961) Theories on the origin of meteorites. J. Chem. Educ 38, 58.

Archer GJ, Ash RD, Bullock ES and Walker RJ (2014) Highly siderophile elements and $^{187}$Re–$^{187}$Os isotopic systematics of the Allende meteorite: evidence for primary nebular processes and late-stage alteration. Geochim. Cosmochim. Acta 131, 402–414.

Arndt NT and Fleet ME (1979) Stable and metastable pyroxene crystallization in layered komatiite lava flows. Am. Mineral 64, 856–864.

Ballhaus C, Berry RF and Green DH (1991) High pressure experimental calibration of the olivine-orthopyroxene-spinel oxygen geobarometer: implications for the oxidation state of the upper mantle. Contrib. Mineral. Petrol 107, 27–40.

Barrat JA, Jambon A, Bohn M, Blichert-Toft J, Sautter V, Göpel C, l Ph., Boudouma O and Keller F (2003) Petrology and geochemistry of the unbrecciated achondrite Northwest Africa 1240 (NWA 1240): an HED parent body impact melt. Geochim. Cosmochim. Acta 67, 3959–3970.

Barnes S-J, Naldrett AJ and Gorton MP (1985) The origin of the fractionation of platinum-group elements in terrestrial magmas. Chem. Geol 53, 302–323.

Becker H, Morgan JW, Walker RJ, MacPherson GL and Grossman JN (2001) Rhenium–osmium systematics of calcium–aluminum-rich inclusions in carbonaceous chondrites. Geochim. Cosmochim. Acta 65, 3379–3390.

Bédard JH (2007) Trace element partitioning coefficients between silicate melts and orthopyroxene: parameterizations of D variations. Chem. Geol 244, 263–303.

Benedix GK, McCoy TJ, Keil K, Bogard DD and Garrison DH (1998) A petrologic and isotopic study of winonaites: evidence for early partial melting, brecciation, and metamorphism. Geochim. Cosmochim. Acta 62, 2535–2553.

Benedix GK, Lauretta DS and McCoy TJ (2005) Thermodynamic constraints on the formation conditions of winonaites and silicate-bearing IAB irons. Geochim. Cosmochim. Acta 69, 5123–5131.

Birck JL, Barman MR and Capmas F (1997) Re–Os isotopic measurements at the femtomole level in natural samples. Geostandards Geoanal. Res 21, 19–27.

Bonnand P, Parkinson IJ and Anand M (2016) Mass dependent fractionation of stable chromium isotopes in mare basalts: implications for the formation and the differentiation of the Moon. Geochim. Cosmochim. Acta 175, 208–221.

Borisov A and Palme H (1995) The solubility of iridium in silicate melts: new data from experiments with $Ir_{10}Pt_{90}$ alloys. Geochim. Cosmochim. Acta 59, 481–485.

Brandon AD, Humayun M and Puchtel IS (2005) Re–Os isotopic systematics and platinum group element concentration of the Tagish Lake carbonaceous chondrite. Geochim. Cosmochim. Acta 69, 1619–1631.

Brandon AD, Puchtel IS, Walker RJ, Day JMD, Irving AJ and Taylor LA (2012) Evolution of the martian mantle inferred from the $^{187}Re$–$^{187}Os$ isotope and highly siderophile element abundance systematics of shergottite meteorites. Geochim. Cosmochim. Acta 76, 206–235.

Brearley AJ (1991) Subsolidus microstructures and cooling history of pyroxenes in the Zagami shergottite Lunar Planet. Sci. XXII, Lunar Planet. Inst., Houston #135 (abstract).

Budde G, Burkhardt C, Brennecka GA, Fischer-Gödde M, Kruijer TS and Kleine T (2016) Molybdenum isotopic evidence for the origin of chondrules and a distinct genetic heritage of carbonaceous and non-carbonaceous meteorites. Earth Planet. Sci. Lett 454, 293–303.

Capobianco CJ, Jones JH and Drake MJ (1993) Metalsilicate thermochemistry at high temperature: magma oceans and the “excess siderophile element” problem of the Earth’s Upper Mantle. J. Geophys. Res 98, 5433–5443.

Carlson RW and Hauri EH (2001) Extending the $^{107}Pd$–$^{107}Ag$ chronometer to low Pd/Ag meteorites with multicollector plasma-ionization mass spectrometry. Geochim. Cosmochim. Acta 65, 1839–1848.

Choi BG, Huss GR, Wasserburg GJ and Gallino R (1998) Presolar corundum and spinel in ordinary chondrites: origins from AGB stars and a supernova. Science 282, 1284–1289. [PubMed: 9812886]

Clayton RN (2002) Solar System: self-shielding in the solar nebula. Nature 415, 860–861.

Clayton RN, Mayeda TK, Goswami JN and Olsen EJ (1991) Oxygen isotope studies of ordinary chondrites. Geochim. Cosmochim. Acta 55, 2317–2337.

Clayton RN and Mayeda TK (1996) Oxygen isotope studies of achondrites. Geochim. Cosmochim. Acta 60, 1999–2017.

Clayton RN and Mayeda TK (1999) Oxygen isotope studies of carbonaceous chondrites. Geochim. Cosmochim. Acta 63, 2089–2104.

Cody AM and Cody RD (1995) Dendrite formation by apparent repeated twinning of calcium oxalate dihydrate. J. Cryst. Growth 151, 369–374.

Cohen AS and Waters FG (1996) Separation of osmium from geological materials by solvent extraction for analysis by thermal ionisation mass spectrometry. Anal. Chim. Acta 332, 269–275.

Creaser RA, Papanastassiou DA, and Wasserburg GJ (1991) Negative thermal ion mass spectrometry of osmium, rhenium and iridium. Geochim. Cosmochim. Acta, 55, 397–401.

Dauphas N and Schauble EA (2016) Mass fractionation laws, mass-independent effects, and isotopic anomalies. Ann. Rev. Earth Planet. Sci 44, 709–783.

Dauphas N, Remusat L, Chen JH, Roskosz M, Papanastassiou DA, Stodolna J, Guan Y, Ma C and Eiler JM (2010) Neutron-rich chromium isotope anomalies in supernova nanoparticles. Astrophys. J 720, 1577.

Dauphas N, Poitrasson F, Burkhardt C, Kobayashi H and Kurosawa K (2015) Planetary and meteoritic Mg/Si and $\delta^{30}Si$ variations inherited from solar nebula chemistry. Earth Planet. Sci. Lett 427, 236–248.

Day JMD, Ash RD, Liu Y, Bellucci JJ, Rumble IIID, McDonough WF, Walker RJ and Taylor LA (2009) Early formation of evolved asteroidal crust. Nature 457, 179–182. [PubMed: 19129845]

Day JMD, Pearson DG, Macpherson CG, Lowry D and Carracedo JC (2010) Evidence for distinct proportions of subducted oceanic crust and lithosphere in HIMU-type mantle beneath El Hierro and La Palma, Canary Islands. Geochim. Cosmochim. Acta 74, 6565–6589.

Day JMD, Walker RJ, Ash RD, Liu Y, Rumble IIID, Irving AJ, Goodrich CA, Tait K, McDonough WF and Taylor LA (2012) Origin of felsic achondrites Graves Nunataks 06128 and 06129, and ultramafic brachinites and brachinite-like achondrites by partial melting of volatile-rich primitive parent bodies. Geochim. Cosmochim. Acta 81, 94–128.

Day JMD (2015) Planet formation processes revealed by meteorites. Geol. Today 31, 12–20.

Day JMD, Corder CA, Rumble D, Assayag N, Cartigny P and Taylor LA (2015) Differentiation processes in FeO-rich asteroids revealed by the achondrite Lewis Cliff 88763. Meteoritics Planet. Sci 50, 1750–1766.

Durant DG and Fowler AD (2002) Origin of reverse zoning in branching orthopyroxene and acicular plagioclase in orbicular diorite, Fisher Lake, California. Mineral. Mag 66, 1003–1020.

Fabriés J (1979) Spinel-olivine geothermometry in peridotites from ultramafic complexes. Contrib. Mineral. Petrol 69, 329–336.

Fernandes VA, Burgess R, Crowther SA, Fritz JP, Gilmour JD, Irving A, Meier MMM, Nottingham M and Wieler R (2013) 40Ar-39Ar and Noble Gas Systematics of the Ungrouped Achondrite Northwest Africa 6704 Lunar Planet. Sci. XLIV, Lunar Planet. Inst., Houston #1956 (abstract).

Fischer-Gödde M, Becker H and Wombacher F (2010) Rhodium, gold and other highly siderophile element abundances in chondritic meteorites. Geochim. Cosmochim. Acta 74, 356–379.

Fitoussi C, Bourdon B, Kleine T, Oberli F and Reynolds BC (2009) Si isotope systematics of meteorites and terrestrial peridotites: implications for Mg/Si fractionation in the solar nebula and for Si in the Earth's core. Earth Planet. Sci. Lett 287, 77–85.

Fleet ME and MacRae ND (1975) A spinifex rock from Munro Township, Ontario. Can. J. Earth Sci 12, 928–939.

Floss C, Crozaz G, Jolliff B, Benedix G and Colton S (2008) Evolution of the winonaite parent body: clues from silicate mineral trace element distributions. Meteoritics Planet. Sci 43, 657–674.

Fortenfant SS, Günther D, Dingwell DB and Rubie DC (2003) Temperature dependence of Pt and Rh solubilities in a haplobasaltic melt. Geochim. Cosmochim. Acta 67, 123–131.

Franchi IA, Wright IP, Sexton AS and Pillinger CT (1999) The oxygen-isotopic composition of Earth and Mars. Meteoritics Planet. Sci 34, 657–661.

Friedrich JM, Wang M-S and Lipschutz ME (2002) Comparison of the trace element composition of Tagish Lake with other primitive carbonaceous chondrites. Meteoritics Planet. Sci 37, 677–686.

Fritz J, Greshake A and Fernandes VA (2017) Revising the shock classification of meteorites. Meteoritics Planet. Sci 52(6), 1216–1232.

Ganguly J and Tazzoli V (1994) $Fe^{2+}$-Mg interdiffusion in orthopyroxene. Am. Mineral 79, 930–937.

Gardner-Vandy KG, Lauretta DS, Greenwood RC, McCoy TJ, Killgore M and Franchi IA (2012) The Tafassasset primitive achondrite: insights into initial stages of planetary differentiation. Geochim. Cosmochim. Acta 85, 142–159.

Goodrich CA (1992) Ureilites-a critical review. Meteoritics 27, 327–352.

Goodrich CA and Delaney JS (2000) Fe/Mg–Fe/Mn relations of meteorites and primary heterogeneity of primitive achondrite parent bodies. Geochim. Cosmochim. Acta 64, 149–160.

Göpel C and Birck JL (2010) Mn/Cr systematics: a tool to discriminate the origin of primitive meteorites. Goldschmidt Conference #348 (abstract).

Göpel C, Birck JL, Galy A, Barrat JA and Zanda B (2015) Mn–Cr systematics in primitive meteorites: insights from mineral separation and partial dissolution. Geochim. Cosmochim. Acta 156, 1–24.

Graham AL, Easton AJ and Hutchison R (1977) Forsterite ehondrites; the meteorites Kakangari, Mount Morris (Wisconsin), Pontlyfiri, and Winona. Mineral. Mag 41, 201–210.

Greenwood RC and Franchi IA (2004) Alteration and metamorphism of CO3 chondrites: evidence from oxygen and carbon isotopes. Meteoritics Planet. Sci. Arch 39, 1823–1838.

Greenwood RC, Franchi IA, Jambon A and Buchanan PC (2005) Widespread magma oceans on asteroidal bodies in the early Solar System. Nature 435, 916–918. [PubMed: 15959509]

Greenwood RC, Franchi IA, Kearsley AT and Alard O (2010) The relationship between CK and CV chondrites. Geochim. Cosmochim. Acta 74, 1684–1705.

Greenwood RC, Franchi IA, Gibson JM and Benedix GK (2012) Oxygen isotope variation in primitive achondrites: the influence of primordial, asteroidal and terrestrial processes. Geochim. Cosmochim. Acta 94, 146–163.

Harju ER, Rubin AE, Ahn I, Choi BG, Ziegler K and Wasson JT (2014) Progressive aqueous alteration of CR carbonaceous chondrites. Geochim. Cosmochim. Acta 139, 267–292.

Hewins RH and Zanda B (2012) Chondrules: precursors and interactions with the nebular gas. Meteoritics Planet. Sci 47, 1120–1138.

Horai K and Winkler J (1974) Thermal Diffusivity of Lunar Rock Sample 12001, 85 Lunar Planet. Sci. VI, Lunar Planet. Inst., Houston pp. 354–356 (abstract).

Horan MF, Walker RJ, Morgan JW, Grossman JN and Rubin A (2003) Highly siderophile elements in chondrites. Chem. Geol 196, 5–20.

Irving AJ, Tanaka R, Steele A, Kuehner SM, Bunch TE, Wittke JH and Hupé GM (2011) Northwest Africa 6704: a unique cumulate permafic achondrite containing sodic feldspar, awaruite and “fluid” inclusions, with an oxygen isotopic composition in the acapulcoite-lodranite field. In 74th Annual Meteoritical Society Meeting, #5231.

Jagoutz E, Palme H, Baddenhausen H, Blum K, Cendales M, Dreibus G, Spettel B, Lorenz V and Wänke H (1979) The abundances of major, minor and trace elements in the earth’s mantle as derived from primitive ultramafic nodules. In Lunar and Planetary Science Conference Proceedings (Vol. 10, pp. 2031–2050).

Jambon A, Humayun M and Barrat JA (2012) Northwest Africa 6693: a unique achondritic cumulate. In Lunar and Planetary Science Conference Proceedings (Vol. 43, #2099).

Jarosewich E (1971) Chemical analysis of the Murchison Meteorite. Meteoritics 6, 49–52.

Jessberger EK, Christoforidis A and Kissel J (1988) Aspects of the major element composition of Halley’s dust. Nature 332, 691–695.

Jochum KP, Weis U, Schwager B, Stoll B, Wilson SA, Haug GH, Andreae MO and Enzwiler J (2015) Reference values following ISO guidelines for frequently requested rock reference materials. Geostandards Geoanal. Res 40, 333–350.

Keil K (2014) Brachinite meteorites: partial melt residues from an FeO-rich asteroid. Chemie der Erde-Geochemistry 74, 311–329.

Keil K and McCoy TJ (in press) Acapulcoite-lodranite meteorites: ultramafic asteroidal partial melt residues. Chemie der Erde-Geochemistry, 10.1016/j.chemer.2017.04.004.

Kennedy AK, Lofgren GE and Wasserburg GJ (1993) An experimental study of trace element partitioning between olivine, orthopyroxene and melt in chondrules: equilibrium values and kinetic effects. Earth Planet. Sci. Lett 115, 177–195.

Kimura K, Lewis RS and Anders E (1974) Distribution of gold and rhenium between nickel– iron and silicate melts: implications for the abundance of siderophile elements on the Earth and Moon. Geochim. Cosmochim. Acta 38, 683–701.

Kleine T, Mezger K, Münker C, Palme H and Bischoff A (2004) $^{182}$Hf-$^{182}$W isotope systematics of chondrites, Eucrites, and Martian meteorites: chronology of core formation and early mantle differentiation in Vesta and Mars. Geochim. Cosmochim. Acta 68, 2935–2946.

Kööp L, Davis AM, Nakashima D, Park C, Krot AN, Nagashima K, Tenner TJ, Heck PR and Kita NT (2016) A link between oxygen, calcium and titanium isotopes in $^{26}$Al-poor hibonite-rich CAIs from Murchison and implications for the heterogeneity of dust reservoirs in the solar nebula. Geochim. Cosmochim. Acta 189, 70–95.

Kon Y and Hirata T (2015) Determination of 10 major and 34 trace elements in 34 GSJ geochemical reference samples using femtosecond laser ablation ICP-MS. Geochem. J 49, 351–375.

Kretz R (1966) Interpretation of the shape of mineral grains in metamorphic rocks. J. Petrol 7, 68–94.

Kruijer TS, Burkhardt C, Budde G and Kleine T (2017) Age of Jupiter inferred from the distinct genetics and formation times of meteorites. Proc. Natl. Acad. Sci 114, 6712–6716. [PubMed: 28607079]

Larsen KK, Trinquier A, Paton C, Schiller M, Wielandt D, Ivanova MA, Connelly JN, Nordlund Å, Krot AN and Bizzarro M (2011) Evidence for magnesium isotope heterogeneity in the solar protoplanetary disk. Astrophys. J. Lett 735, 37–44.

Larimer JW (1979) The condensation and fractionation of refractory lithophile elements. Icarus 40, 446–454.

Laubier M, Grove TL and Langmuir CH (2014) Trace element mineral/melt partitioning for basaltic and basaltic andesitic melts: an experimental and laser ICP-MS study with application to the oxidation state of mantle source regions. Earth Planet. Sci. Lett 392, 265–278.

Le Corre L, Reddy V, Cloutis EA, Mann P, Buchanan PC Gabelica Z, Hupé G and Gaffey MJ (2014) Identifying Parent Asteroid of Ungrouped Achondrite Northwest Africa 6704: lessons from Dawn at Vesta Lunar Planet. Sci. XLV, Lunar Planet. Inst., Houston #1311 (abstract).

Leya I, Schönbächler M, Wiechert U, Krähenbühl U and Halliday AN (2007) High precision titanium isotope measurements on geological samples by high resolution MC-ICPMS. Int. J. Mass Spectrom 262, 247–255.

Leya I, Schonbachler M, Wiechert U, Krahenbuhl U and Halliday AN (2008) Titanium isotopes and the radial heterogeneity of the solar system. Earth Planet. Sci. Lett 266, 233–244.

Lindsley DH and Andersen DJ (1983) A two-pyroxene thermometer. J. Geophys. Res.: Solid Earth, 88.

Lodders K (2003) Solar system abundances and condensation temperatures of the elements. Astrophys. J 591, 1220–1247.

Lofgren GE (1980) Experimental studies on the dynamic crystallization of silicate melts In Physics of Magmatic Process (ed. Hargrave RB). Princeton University Press, Princetonpp. 487–551.

Ludwig KR (2001) Users Manual for Isoplot/Ex version 2.47 A geochronological toolkit for Microsoft Excel. Berkeley Geochronology Center Special Publication 1a, 55pp.

Lyons JR and Young ED (2005) CO self-shielding as the origin of oxygen isotope anomalies in the early solar nebula. Nature 435, 317–320. [PubMed: 15902251]

Makishima A and Nakamura E (2006) Determination of Major, Minor and Trace Elements in Silicate Samples by ICP-QMS and ICP-SFMS Applying Isotope Dilution-Internal Standardisation (ID-IS) and Multi-Stage Internal Standardisation. Geostandards Geoanal. Res 30, 245–271.

Mann U, Frost DJ, Rubie DC, Becker H and Audétat A (2012) Partitioning of Ru, Rh, Pd, Re, Ir and Pt between liquid metal and silicate at high pressures and temperatures – implications for the origin of highly siderophile element concentrations in the Earth's mantle. Geochim. Cosmochim. Acta 84, 593–613.

Mason B (1967) Meteorites. American Scientist 55, 429–455.

McCoy TJ, Keil K, Clayton RN and Mayeda TK (1993) Classificational parameters for acapulcoites and lodranites: the cases of FRO 90011, EET 84302 and ALH A81187/84190 Lunar Planet. Sci. XXIV, Lunar Planet. Inst., Houston #945 (abstract).

McCoy TJ, Keil K, Clayton RN, Mayeda TK, Bogard DD, Garrison DH, Huss GR, Hutcheon ID and Wieler R (1996) A petrologic, chemical, and isotopic study of Monument Draw and comparison with other acapulcoites: evidence for formation by incipient partial melting. Geochim. Cosmochim. Acta 60, 2681–2708.

McSween HY (1987) Aqueous alteration in carbonaceous chondrites: mass balance constraints on matrix mineralogy. Geochimica et Cosmochimica Acta 51, 2469–2477.

Mittlefehldt DW, Lindstrom MM, Bogard DD, Garrison DH and Field SW (1996) Acapulco-and Lodran-like achondrites: petrology, geochemistry, chronology, and origin. Geochim. Cosmochim. Acta 60, 867–882.

Mittlefehldt DW, McCoy TJ, Goodrich CA and Kracher A (1998) Non-chondritic meteorites from asteroidal bodies. In Planetary Materials, vol. 36 (ed. Papike JJ). Rev. Mineralogy, pp. 4–1–4–195.

Newsom HE (1990) Accretion and core formation in the Earth: evidence from siderophile elements In Origin of the Earth (eds. Newsom HE and Jones JH). Oxford Univ. Press, New York, pp. 273–288.

Newton J, Franchi IA and Pillinger CT (2000) The oxygen isotopic record in enstatite meteorites. Meteoritics Planet. Sci 35, 689–698.

O'Neill HSC, Dingwell DB, Borisov A, Spettel B and Palme H (1995) Experimental petrochemistry of some highly siderophile elements at high temperatures, and some implications for core formation and the mantle's early history. Chem. Geol 120, 255–273.

Ozawa K (1984) Olivine-spinel geospeedometry: analysis of diffusion-controlled Mg-$Fe^{2+}$ exchange. Geochimica et Cosmochimica Acta 48, 2597–2611.

Pack A, Tanaka R, Hering M, Sengupta S, Peters S and Nakamura E (2016) The oxygen isotope composition of San Carlos olivine on the VSMOW2-SLAP2 scale. Rapid Commun. Mass Spectrometry 30, 1495–1504.

Palme H (1981) Abundances of the elements in the solar system. Astron. Astrophys, 257–272.

Palme H (2000) Are there chemical gradients in the inner Solar System? Space Sci. Rev 92, 237–264.

Palme H and Beer H (1993) Abundances of the elements in the Solar System In Landolt Bornstein, group VI: astronomy and astrophysics (ed. Voigt HH), vol. 3 Springerpp. 196–221.

Palme H and O'Neill H (2014) Cosmochemical Estimates of Mantle Composition. In Planets, Asteriods, Comets and The Solar System, Volume 2 of Treatise on Geochemistry (ed. Davis Andrew M.).

Petitat M, Birck JL, Luu TH and Gounelle M (2011) The chromium isotopic composition of the ungrouped carbonaceous chondrite Tagish Lake. The Astrophysical Journal 736, 23.

Prinz M, Waggoner DG and Hamilton PJ (1980) Winonaites: a primitive achondritic group related to silicate inclusions in IAB irons, Lunar Planet. Sci. XI, Lunar Planet. Inst., Houston pp. 902–904 (abstract).

Prinz M, Nehru CE, Delaney JS and Weisberg M (1983) Silicates in IAB and IIICD Irons, Winonaites, Lodranites an Brachina: a Primitive and Modified-Primitive Group Lunar Planet. Sci. XIV, Lunar Planet. Inst., Houston pp. 616–617 (abstract).

Puchtel IS, Humayun M, Campbell AJ, Sproule RA and Lesher CM (2004) Platinum group element geochemistry of komatiites from the Alexo and Pyke Hill areas, Ontario, Canada. Geochim. Cosmochim. Acta 68, 1361–1383.

Puchtel IS, Humayun M and Walker RJ (2007) Os–Pb–Nd isotope and highly siderophile and lithophile trace element systematics of komatiitic rocks from the Volotsk suite, SE Baltic Shield. Precambrian Res. 158, 119–137.

Qin L, Alexander CM and O'D., Carlson RW, Horan MF, and Yokoyama T (2010a) Contributions to chromium isotope variations of meteorites. Geochim. Cosmochim. Acta 74, 1122–1145.

Qin L, Rumble D, Alexander CMOD, Carlson RW, Jenniskens P and Shaddad MH (2010b) The chromium isotopic composition of Almahata Sitta. Meteorit Planet Sci. 45, 1771–1777.

Qin L, Nittler LR, Alexander COD, Wang J, Stadermann FJ and Carlson RW (2011) Extreme $^{54}$Cr-rich nano-oxides in the CI chondrite Orgueil-Implication for a late supernova injection into the solar system. Geochim. Cosmochim. Acta 75, 629–644.

Riches AJ, Day JM, Walker RJ, Simonetti A, Liu Y, Neal CR and Taylor LA (2012) Rhenium–osmium isotope and highly-siderophile-element abundance systematics of angrite meteorites. Earth Planet. Sci. Lett 353, 208–218.

Righter K and Neff KE (2007) Temperature and oxygen fugacity constraints on CK and R chondrites and implications for water and oxidation in the early solar system. Polar Sci. 1, 25–44.

Ringwood AE (1961) Chemical and genetic relationships among meteorites. Geochim. Cosmochim. Acta 24, 159–197.

Rankenburg K, Humayun M, Brandon AD and Herrin JS (2008) Highly siderophile elements in ureilites. Geochim. Cosmochim. Acta 72, 4642–4659.

Rehkämper M and Halliday AN (1997) Development and application of new ion-exchange techniques for the separation of the platinum group and other siderophile elements from geological samples. Talanta 44, 663–672. [PubMed: 18966788]

Rubin AE (2006) Shock, post-shock annealing, and postannealing shock in ureilites. Meteoritics Planet. Sci 41, 125–133.

Rubin AE (2007) Petrogenesis of acapulcoites and lodranites: a shock-melting model. Geochim. Cosmochim. Acta 71, 2383–2401.

Rubin AE (2011) Origin of the differences in refractorylithophile-element abundances among chondrite groups. Icarus 213, 547–558.

Russell WA, Papanastassiou DA and Tombrello TA (1978) Ca isotope fractionation on the Earth and other solar system materials. Geochim. Cosmochim. Acta 42, 1075–1090.

Sanborn ME and Yin QZ (2015) Investigating a Common Source for Brachinites and Graves Nunataks 06128 and 06129 Meteorites Using High Precision Chromium Isotopes Lunar Planet. Sci. XLVI, Lunar Planet. Inst., Houston #2241 (abstract).

Sanborn ME, Yin Q-Z and Irving AJ (2014) Isotope forensics utilizing D17O-e54Cr systematics provide supporting evidence for differentiated bodies overlain by chondritic veneers: a case for the CR parent body Lunar Planet. Sci. XLV, Lunar Planet. Inst., Houston #2032 (abstract).

Sanborn ME, Wimpenny J, Williams CD, Yamakawa A, Amelin Y, Irving AJ and Yin Q-Z (2019) Carbonaceous achondrites Northwest Africa 6704/6693: new anchors for early solar system chronology and genealogy. Geochim. Cosmochim. Acta 245, 577–596.

Schiller M, Van Kooten E, Holst JC, Olsen MB and Bizzarro M (2014) Precise measurement of chromium isotopes by MCICPMS. J. Anal. Atomic Spectrom 29, 1406–1416.

Schmitz B, Yin Q-Z, Sanborn ME, Tassinari M, Caplan C and Huss G (2016) A new type of solar-system material recovered from Ordovician marine limestone. Nat. Commun 7, 11851.

Schoenberg R, Merdian A, Holmden C, Kleinhanns IC, Haßler K, Wille M and Reitter E (2016) The stable Cr isotopic compositions of chondrites and silicate planetary reservoirs. Geochim. Cosmochim. Acta 183, 14–30.

Schrader DL, Franchi IA, Connolly HC, Greenwood RC, Lauretta DS and Gibson JM (2011) The formation and alteration of the Renazzo-like carbonaceous chondrites I: implications of bulk-oxygen isotopic composition. Geochim. Cosmochim. Acta 75, 308–325.

Schramm LS, Brownlee DE and Wheelock MM (1989) Major element composition of stratospheric micrometeorites. Meteoritics 24, 99–112.

Schulze H, Bischoff A, Palme H, Spettel B, Dreibus G and Otto J (1994) Mineralogy and chemistry of Rumuruti: the first meteorite fall of the new R chondrite group. Meteoritics Planet. Sci 29, 275–286.

Schwartz AJ, Kumar M, Adams BL and Field DP (eds.) (2009) Electron backscatter diffraction in materials science (Vol. 2). Springer, New York.

Scott ER, Greenwood RC, Franchi IA and Sanders IS (2009) Oxygen isotopic constraints on the origin and parent bodies of eucrites, diogenites, and howardites. Geochim. Cosmochim. Acta 73, 5835–5853.

Sharp ZD (1990) A laser-based microanalytical method for the in situ determination of oxygen isotope ratios of silicates and oxides. Geochim. Cosmochim. Acta 54, 1353–1357.

Shirey SB and Walker RJ (1995) Carius tube digestion for low blank rhenium-osmium analysis. Anal. Chem 67, 2136–2141.

Shukolyukov A and Lugmair GW (2006a) Manganese– chromium isotope systematics of carbonaceous chondrites. Earth Planet. Sci. Lett 250, 200–213.

Shukolyukov A and Lugmair GW (2006b) The Mn–Cr isotope systematics in the ureilites Kenna and LEW85440, Lunar Planet. Sci. XXXVII, Lunar Planet. Inst., Houston #1478 (abstract).

Shukolyukov A, Lugmair GW and Irving AJ (2009) Mn-Cr isotope systematics of angrite northwest Africa 4801 Lunar Planet. Sci. XL, Lunar Planet. Inst., Houston #1381 (abstract).

Shukolyukov A, Lugmair GW and Irving AJ (2011) Mn-Cr isotope systematics and excess of 54Cr in metachondrite Northwest Africa 3133 Lunar Planet. Sci. XLII, Lunar Planet. Inst., Houston #1527 (abstract).

Spitz AH and Boynton WV (1991) Trace element analysis of ureilites: new constraints on their petrogenesis. Geochim. Cosmochim. Acta 55, 3417–3430.

Takagi Y, Noguchi T, Kimura M and Yamaguchi A (2014) Crystallization and subsolidus processes of the NWA 6704 ungrouped achondrite. Japan Geoscience Union Meeting 2014, Japan Geoscience Union, Yokohama #PPS22-P03 (abstract).

Tanaka R and Nakamura E (2013) Determination of $^{17}$O-excess of terrestrial silicate/oxide minerals with respect to Vienna Standard Mean Ocean Water (VSMOW). Rapid Commun. Mass Spectrom 27, 285–297. [PubMed: 23239376]

Terashima S, Taniguchi M, Mikoshiba M and Imai N (1998) Preparation of two new GSJ geochemical reference materials: basalt JB-1b and coal fly ash JCFA-1. Geostandards Geoanal. Res 22, 113–117.

Tomeoka K and Buseck PR (1985) Indicators of aqueous alteration in CM carbonaceous chondrites: microtextures of a layered mineral containing Fe, S, O and Ni. Geochimica et Cosmochimica Acta 49, 2149–2163.

Touboul M, Kleine T, Bourdon B, Van Orman JA, Maden C and Zipfel J (2009) Hf–W thermochronometry: II. Accretion and thermal history of the acapulcoite–lodranite parent body. Earth Planet. Sci. Lett 284, 168–178.

Trinquier A, Birck J−L and Alle`gre C (2007) Widespread $^{54}$Cr heterogeneity in the inner solar system. Astrophys. J 655, 1179–1185.

Trinquier A, Birck JL and Alle`gre CJ (2008) High-precision analysis of chromium isotopes in terrestrial and meteorite samples by thermal ionization mass spectrometry. J. Anal. Atomic Spectrom 23, 1565–1574.

Trinquier A, Elliott T, Ulfbeck D, Coath C, Krot AN and Bizzarro M (2009) Origin of nucleosynthetic isotope heterogeneity in the solar protoplanetary disk. Science 324, 374–376. [PubMed: 19372428]

Tsuchiyama A (1986) Experimental-study of olivine-melt reaction and its petrological implications. J. Volcanol. Geotherm. Res 29, 245–264.

Van Kooten EM, Wielandt D, Schiller M, Nagashima K, Thomen A, Larsen KK, Olsen MB, Nordlund A, Krot AN and Bizzarro M (2016) Isotopic evidence for primordial molecular cloud material in metal-rich carbonaceous chondrites. Proc. Natl. Acad. Sci 113, 2011–2016. [PubMed: 26858438]

Vernon RH (1968) Microstructures of high-grade metamorphic rocks at Broken Hill, Australia. J. Petrol 9, 1–22.

Vernon RH (1970) Comparative grain-boundary studies of some basic and ultrabasic granulites, nodules and cumulates. Scottish J. Geol 6, 337–351.

Vetere F, Iezzi G, Behrens H, Holtz F, Ventura G, Misiti V, Cavallo A, Mollo S and Dietrich M (2015) Glass forming ability and crystallisation behaviour of sub-alkaline silicate melts. Earth-Sci. Rev 150, 25–44.

Walton EL and Herd CD (2007) Dynamic crystallization of shock melts in Allan Hills 77005: implications for melt pocket formation in Martian meteorites. Geochim. Cosmochim. Acta 71, 5267–5285.

Walker RJ, Storey M, Kerr AC, Tarney J and Arndt NT (1999) Implication of $^{187}$Os isotopic heterogeneities in a mantle plume: evidence from Gorgona Island and Curacao. Geochim. Cosmochim. Acta 63, 713–728.

Walker RJ, Horan MF, Morgan JW, Becker H, Grossman JN and Rubin A (2002) Comparative $^{187}$Re–$^{187}$Os systematics of chondrites: implications regarding early solar system processes. Geochim. Cosmochim. Acta 66, 4187–4201.

Walsh KJ, Morbidelli A, Raymond SN and O'brien DP, and Mandell AM (2011) A low mass for Mars from Jupiter/'s early gas-driven migration. Nature 475, 206–209. [PubMed: 21642961]

Warren PH, Ulff-Møller F, Huber H and Kallemeyn GW (2006) Siderophile geochemistry of ureilites: a record of early stages of planetesimal core formation. Geochimica et Cosmochimica Acta 70, 2104–2126.

Warren PH (2011) Stable-isotopic anomalies and the accretionary assemblage of the Earth and Mars: a subordinate role for carbonaceous chondrites. Earth Planet. Sci. Lett 311, 93–100.

Warren PH and Rubin AE (2010) Pyroxene-selective impact smelting in ureilites. Geochim. Cosmochim. Acta 74, 5109–5133.

Warren PH, Rubin AE, Isa J, Brittenham S, Ahn I and Choi B-G (2013) Northwest Africa 6693: a new type of FeO-rich, low-$\Delta^{17}$O, poikilitic cumulate achondrite. Geochim. Cosmochim. Acta 107, 135–154.

Wasson JT and Kallemeyn GW (1988) Compositions of chondrites. Philos. Trans. R. Soc. Lond. A: Math. Phys. Eng. Sci 325, 535–544.

Weisberg MK, McCoy TJ and Krot AN (2006) Systematics and evaluation of meteorite classification, In, Meteorites and the Early Solar System II (eds. Lauretta DS and McSween HY Jr.). University of Arizona Press, Tucsonpp.19–52.

Weiss BP and Elkins-Tanton LT (2013) Differentiated planetesimals and the parent bodies of chondrites. Ann. Rev. Earth Planet. Sci 41, 529–560.

Welsch B, Faure F, Famin V, Baronnet A and Bache`lery P (2012) Dendritic crystallization: a single process for all the textures of olivine in basalts?. J. Petrol, egs077.

Wiechert U, Halliday AN, Lee DC, Snyder GA, Taylor LA and Rumble D (2001) Oxygen isotopes and the Moon-forming giant impact. Science 294, 345–348. [PubMed: 11598294]

Wiechert UH, Halliday AN, Palme H and Rumble D (2004) Oxygen isotope evidence for rapid mixing of the HED meteorite parent body. Earth Planet. Sci. Lett 221, 373–382.

Wiik HB (1972) The chemical composition of the Haverö meteorite and the genesis of the ureilites. Meteoritics 7, 553–558.

Wombacher F and Rehkämper M (2003) Investigation of the mass discrimination of multiple collector ICP-MS using neodymium isotopes and the generalised power law. J. Anal. Atomic Spectrom 18, 1371–1375.

Yamakawa A, Yamashita K, Makishima A and Nakamura E (2009) Chemical separation and mass spectrometry of Cr, Fe, Ni, Zn, and Cu in terrestrial and extraterrestrial materials using thermal ionization mass spectrometry. Anal. Chem 81, 9787–9794. [PubMed: 19886654]

Yamakawa A, Yamashita K, Makishima A and Nakamura E (2010) Chromium isotope systematics of achondrites: chronology and isotopic heterogeneity of the inner solar system bodies. Astrophys. J 720, 150.

Yamashita K, Ueda T, Nakamura N, Kita N and Heaman LM (2005) Chromium isotopic study of mesosiderite and ureilite: evidence for ε54Cr deficit in differentiated meteorites. In NIPR Symp. Antarct. Meteorit (Vol. 29, pp. 100–101).

Young ED and Galy A (2004) The isotope geochemistry and cosmochemistry of magnesium. Rev. Mineral. Geochem 55, 197–230.

Yurimoto H and Kuramoto K (2004) Molecular cloud origin for the oxygen isotope heterogeneity in the solar system. Science 305, 1763–1766. [PubMed: 15375265]

Zhang J, Dauphas N, Davis AM and Pourmand A (2011) A new method for MC-ICPMS measurement of titanium isotopic composition: identification of correlated isotope anomalies in meteorites. J. Anal. At. Spetrom 26, 2197–2205.

Zhang J, Dauphas N, Davis AM, Leya I and Fedkin A (2012) The proto-Earth as a significant source of lunar material. Nat. Geosci 5, 251–255.

**Fig. 1.**
An image of the reassembled mass of NWA 6704 (courtesy of Greg Hupé). The scale cube is 1 $cm^3$.

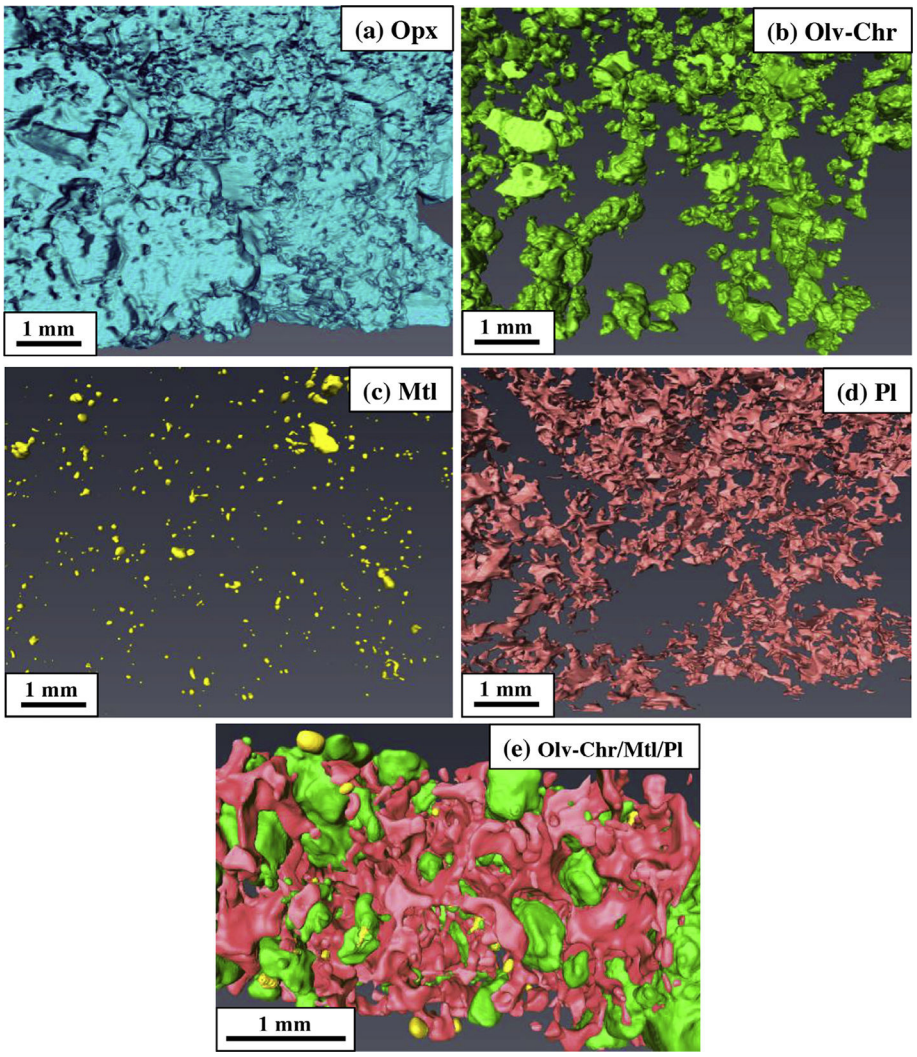


**Fig. 2.**

3D X-ray computed tomography (CT) images of (a) orthopyroxene, (b) olivine-chromite, (c) Fe-Ni metal, (d) plagioclase and (e) minerals other than orthopyroxene: olivine-chromite (green), metal (yellow), and plagioclase (pink).

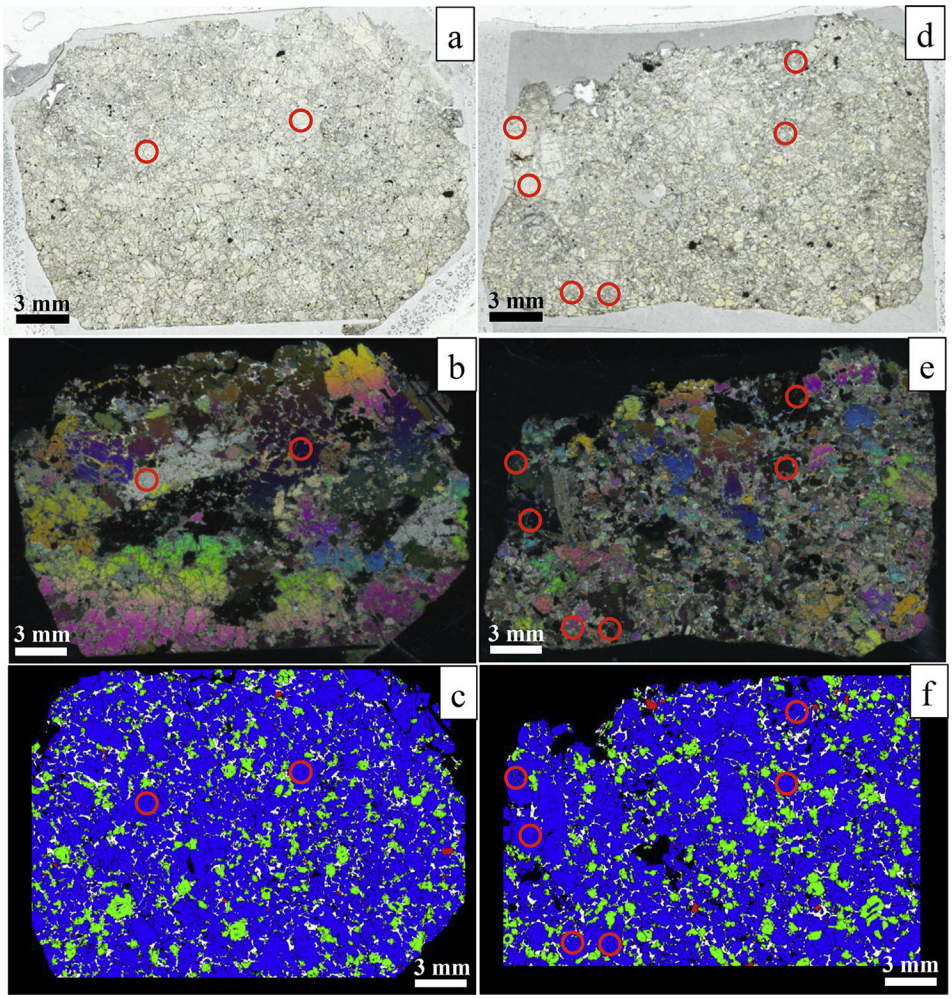


**Fig. 3.**

Scanned images of “coarse-part” (TS-7) and “fine-part” (TS-6) are shown in the left- and right-hand columns, respectively. (a, d) opennicols, (b, e) crossed-nicols and (c, f) chemical maps: orthopyroxene (blue), olivine (green), metal (red), and plagioclase (white). Vermicular olivine inclusions in the core regions of orthopyroxene megacrysts are highlighted by a red circle.

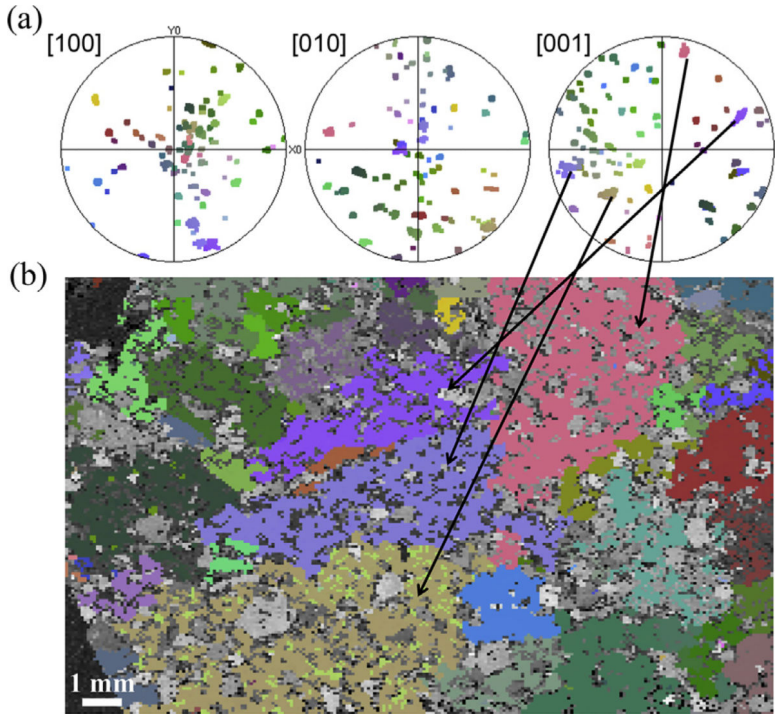


**Fig. 4.**

(a) Pole figure diagrams for orthopyroxene {1 0 0} in thin section TS7. The maps were created with Euler color ascribed to orientations. (b) The inverse pole figure map of the analyzed area. The color of each phase corresponds to the color in obtained crystal orientation stereo nets. It shows that [0 0 1] of orthopyroxene grains correspond to their maximum length axes.

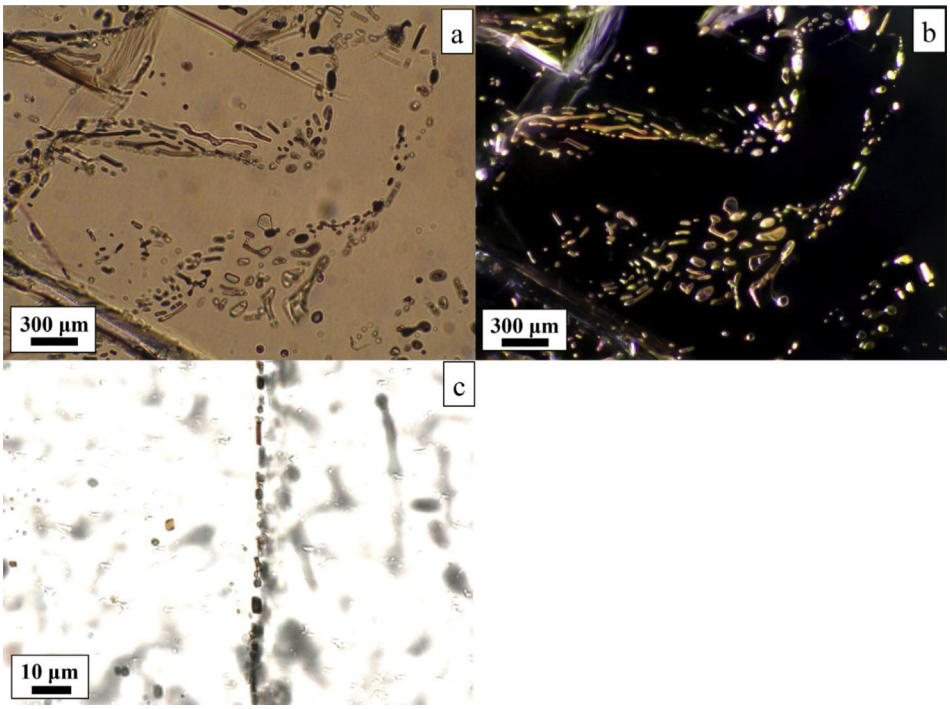


**Fig. 5.**

Optical thin section images of curvilinear trains of micro-inclusions (<2–30 μm) enclosed in some orthopyroxene megacrysts: (a and b) open- and crossed nicol views of rounded to irregularly-shaped clear to pinkish empty bubbles, and (c) open-nicol view of rectangular to oval brownish chromite inclusions.

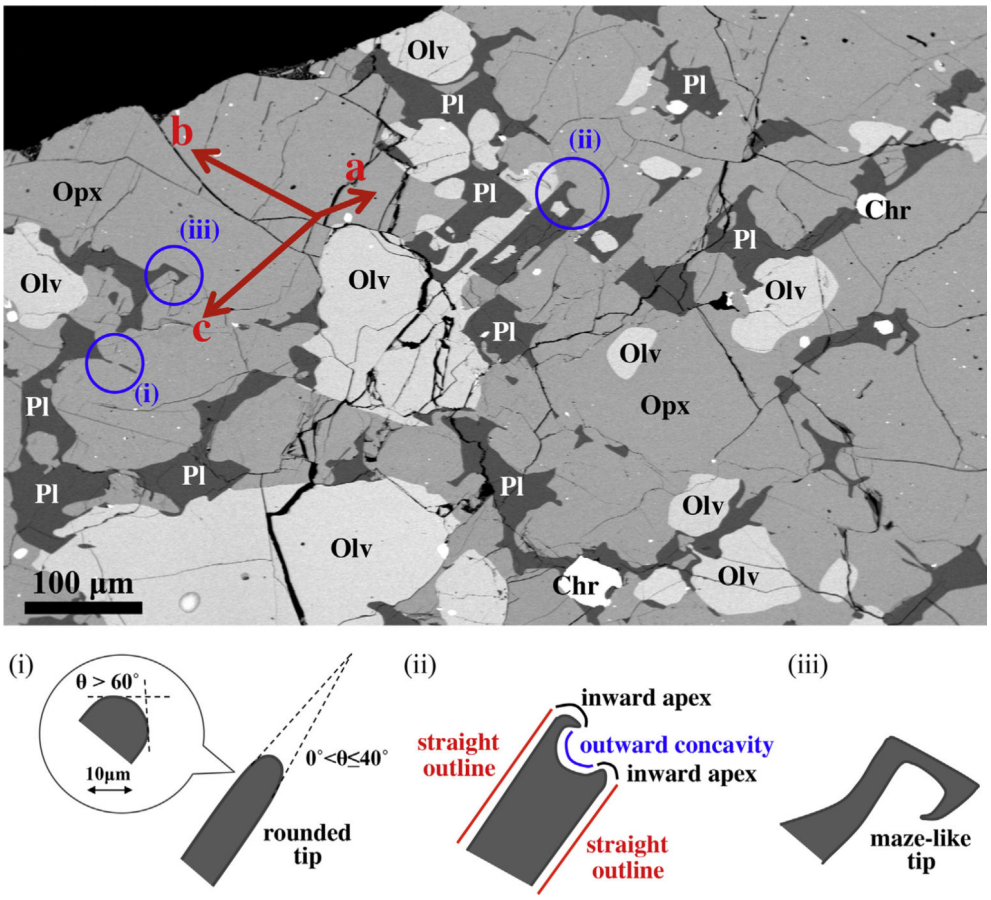


**Fig. 6.**

Back-scattered electron image of thin section TS-7. The [1 0 0], [0 1 0] and [0 0 1] axes of orthopyroxene are compared with the shape of plagioclase, indicating that the shape of plagioclase is controlled by the facets of orthopyroxene megacrysts. Plagioclase typically shows three types of morphology; (i) cuspate shape with extremely low dihedral angles ($0 < \theta \leq 40°$) on the scale greater than ~100 µm, and with much greater than 60° on the scale smaller than ~20 µm, (ii) rectangular morphology with both curvatures and straight interfaces with the host, and (iii) thin, delicate maze-like morphology with or without branches extending into orthopyroxene megacrysts.

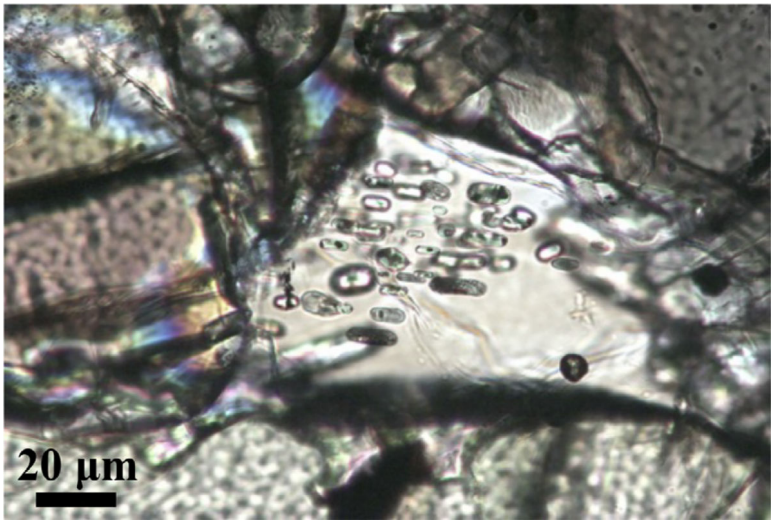


**Fig. 7.**
Reflected-light, crossed-nicol view of oval inclusions in plagioclase of NWA 6704.

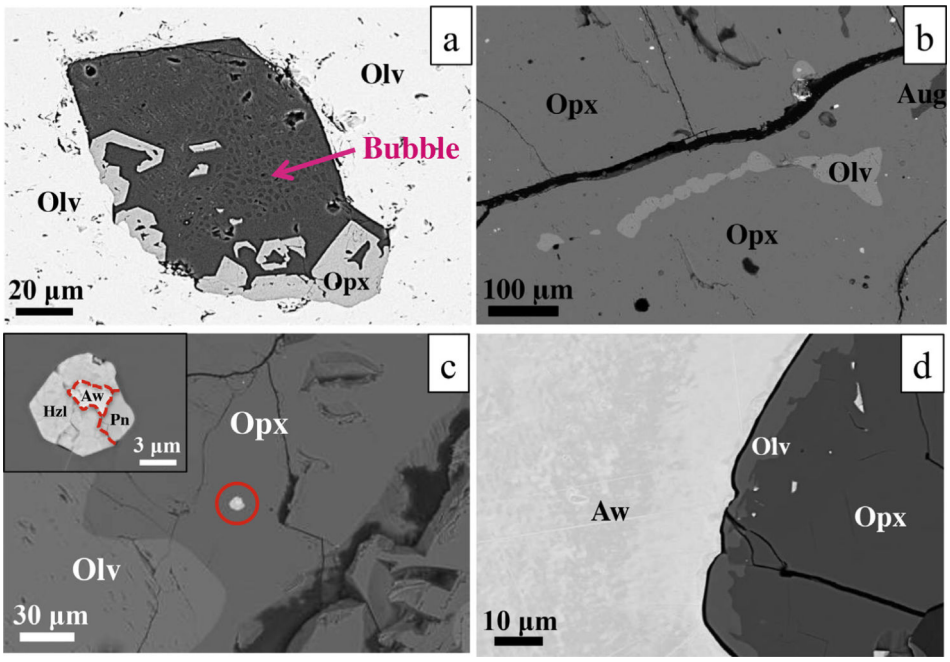


**Fig. 8.**

Backscattered electron images showing (a) a melt inclusion in olivine, composed of skeletal orthopyroxene and glass with bubbles, (b) vermicular olivine inclusions within the orthopyroxene, (c) Fe-Ni-S minerals of awaruite ($Fe_{20}Ni_{80}$) + heazlewoodite ($Fe_2Ni_{56}S_{42}$) + pentlandite ($Fe_{27}Ni_{25}S_{48}$) enclosed by orthopyroxene, and (d) reaction rims of Fe, Ni-rich olivine along the grain boundary between large awaruite and orthopyroxene.

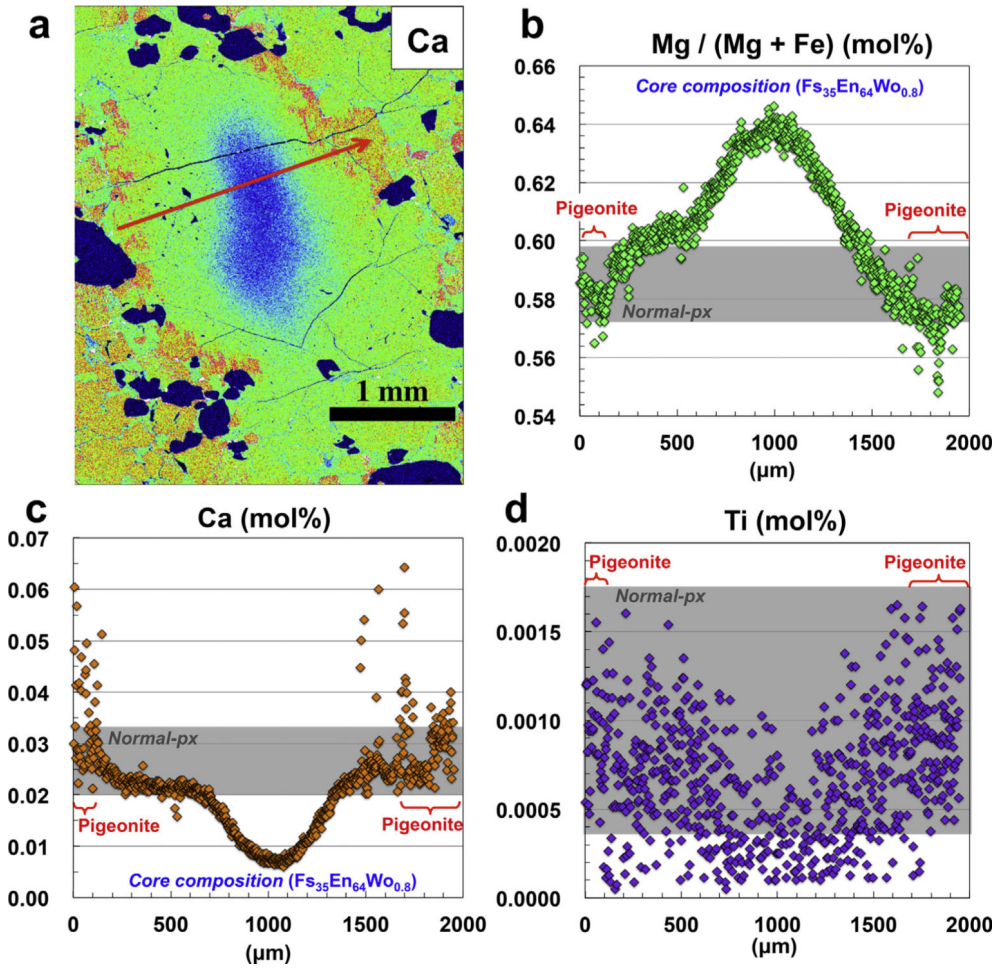


**Fig. 9.**

A chemically zoned orthopyroxene megacryst: (a) Ca-mapping image and line profiles (2 μm step) of (b) Mg#, (c) Ca and (d) Ti. The shaded area (Ca = 0.02–0.03 mol%, Mg# = 57–60) shows the compositional range of “normal” Mg# orthopyroxene, randomly selected pyroxene among the thin section (n = 20). The orthopyroxene is further surrounded by pigeonite having exsolution lamellae of clinopyroxene.

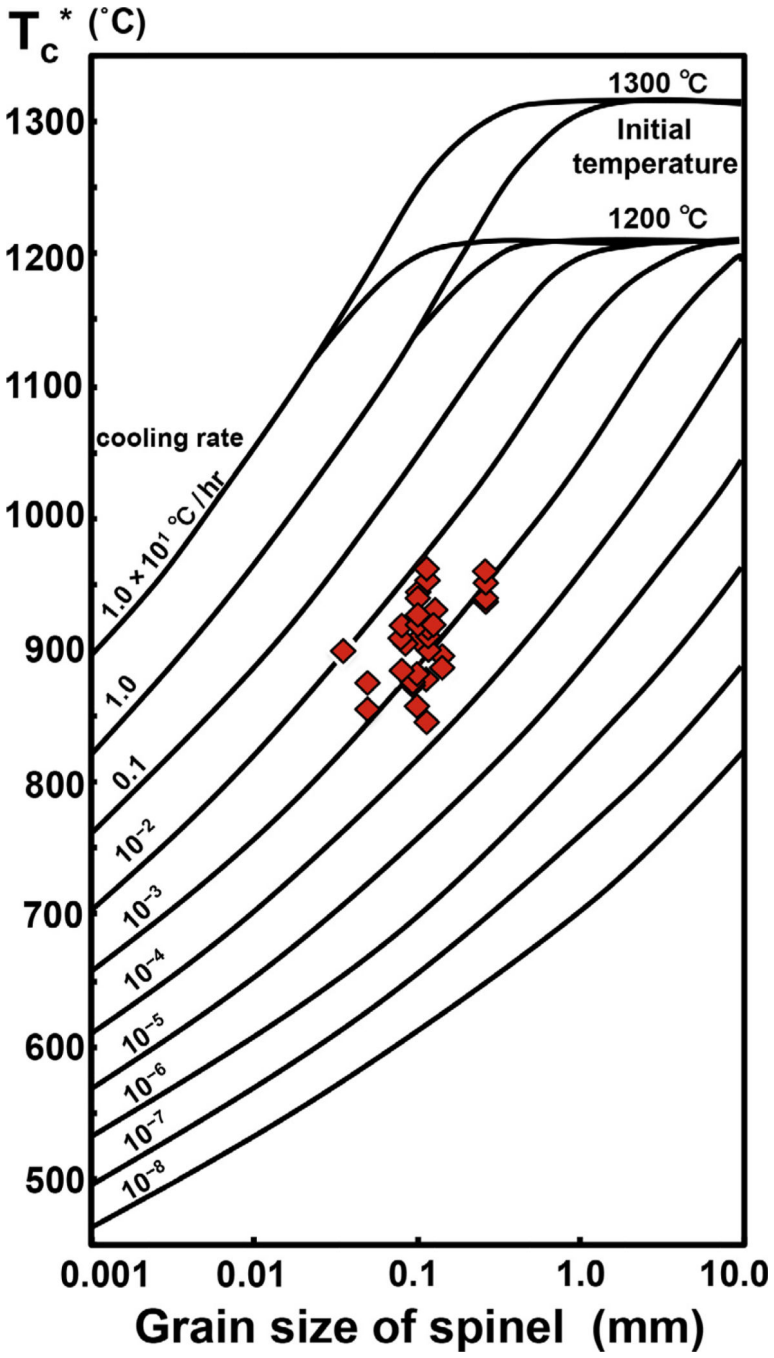


**Fig. 10.**

Plot of estimated temperature (T* c) vs. grain size (usp) for chromite grains of NWA 6704. The T*c usp relationship can be used to constrain the cooling rate based on geospeedometry established by Ozawa (1984). The data for NWA 6704 chromite grains are represented by red points. The T*c were estimated using the olivinespinel Fe-Mg exchange geothermometer of Fabrie´s (1979) for each chromite grain with the neighboring olivine.

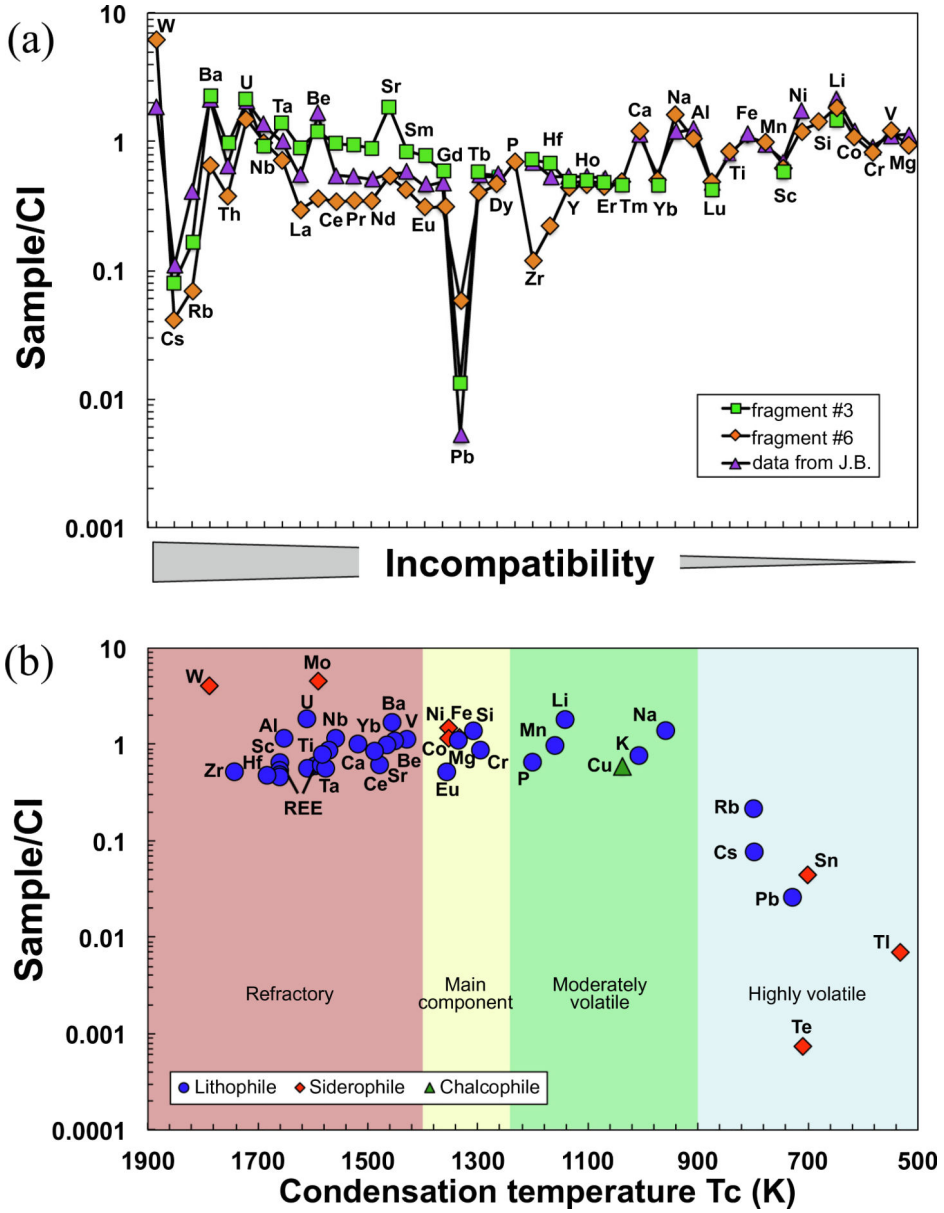


**Fig. 11.**

CI-normalized (Palme and O'Neill, 2014) major and trace element abundances of NWA 6704. (a) The data for whole rock fragments #3 and #6 are plotted against the order of decreasing incompatibility to orthopyroxene (Kennedy et al., 1993; Bédard, 2007; Laubier et al., 2014). The whole rock data obtained by Jean-Alix Barrat (J.B.) are also shown for comparison. (b) The averaged values of the data shown in (a) are plotted against the 50% condensation temperature for a solar composition gas at $10^{-4}$ bar (Tc, Lodders, 2003).

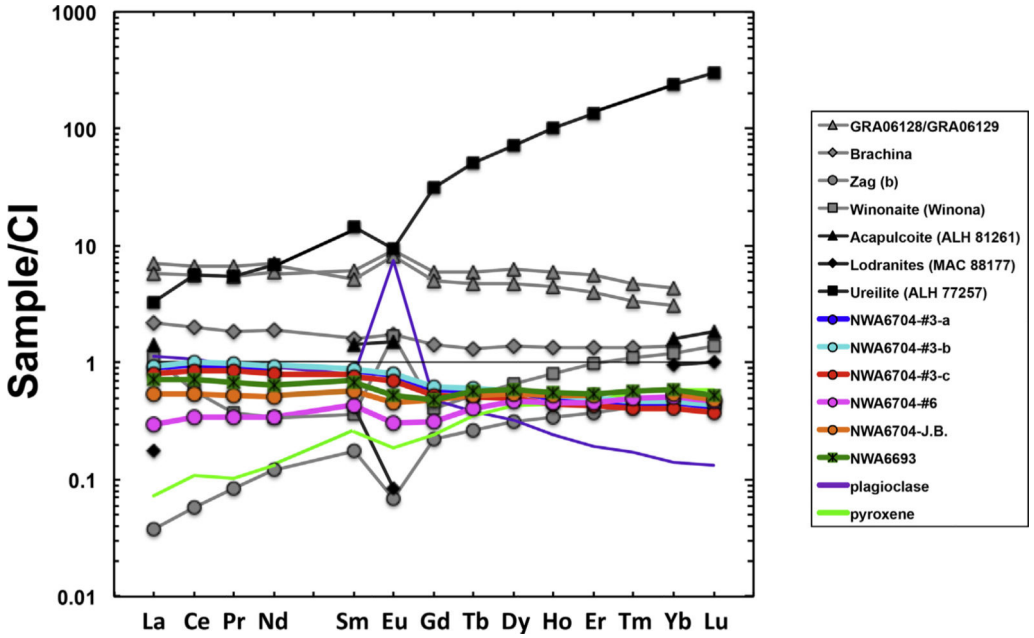


**Fig. 12.**

Comparison of CI-normalized (Palme and O'Neill, 2014) whole rock rare earth element abundances between NWA 6704 and various primitive achondrites (GRA 06128/9, Brachina and Zag from Day et al., 2012; Winona from Floss, 2008; ALH 81261 and MAC 88177 from Mittlefehldt et al., 1996; ALH 77257 from Spitz and Boynton, 1991; NWA 6693 from Warren et al., 2013). NWA6704-J.B. represents the data provided by Jean-Alix Barrat (J.B.). Also shown are rare earth element patterns of plagioclase and pyroxene separates of NWA 6704.

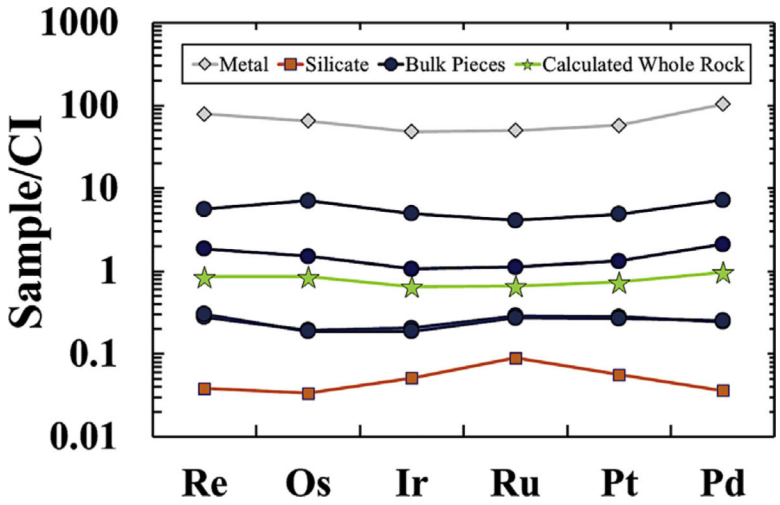


**Fig. 13.**

CI-normalized (Horan et al., 2003) highly siderophile element abundances of NWA 6704 bulk fragments, metal, silicate, and calculated whole rock. Uncertainties are smaller than symbols.

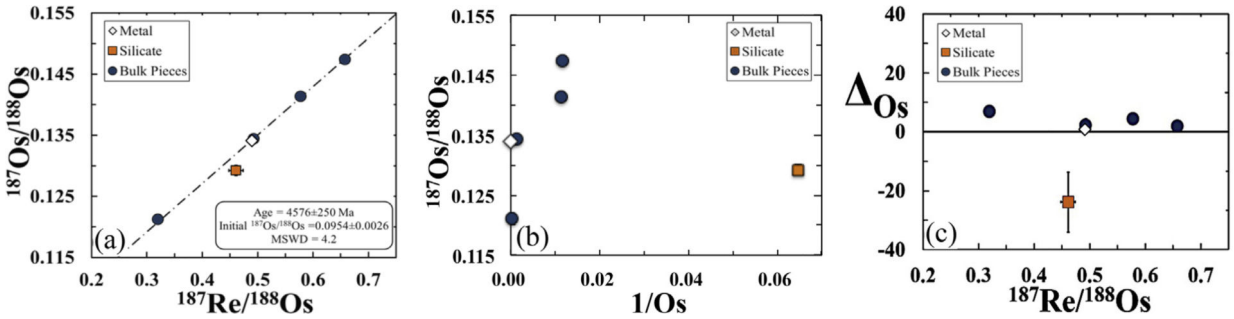


**Fig. 14.**

$^{187}Re$–$^{187}Os$ systematics of NWA 6704 bulk, metal, and silicate fractions. Uncertainties are smaller than symbols unless shown. (a) Re–Os isochron calculated using ISOPLOT (Ludwig, 2001) for NWA 6704 metal and bulk fractions. (b) Plot of $^{187}Os/^{188}Os$ vs. 1/Os. (c) The absolute deviation in parts per 10,000, from a primordial 4568 Ma reference isochron ($\Delta_{Os}$) plotted against $^{187}Re/^{188}Os$.

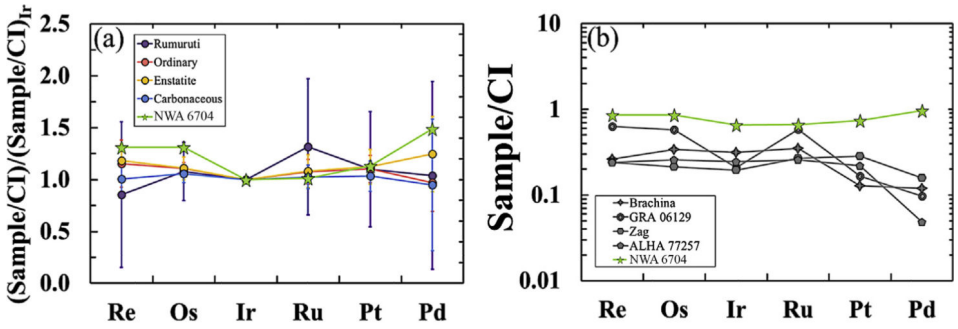


**Fig. 15.**

CI-normalized (Horan et al., 2003) highly siderophile element (HSE) abundances of NWA 6704 whole rock, compared with those of (a) chondrite groups and (b) achondrites. HSE abundances in (a) are doubly normalized to CI chondrites (Horan et al., 2003) and Ir. For comparison, doubly normalized average and 2σ of ordinary, carbonaceous, enstatite, and Rumuruti-like chondrites HSE abundances are also shown in (a). The HSE abundances of NWA 6704 whole rock in (b) are normalized only to CI chondrites (Horan et al., 2003). For comparison, CI-normalized HSE abundances of various primitive achondrites are also shown in (b). The plots for ordinary, carbonaceous, enstatite, and Rumuruti-like chondrites are based on the data reported by Walker et al. (2002), Horan et al. (2003), Brandon et al. (2005), Fischer-Gödde et al. (2010) and Day et al. (2015). Data for GRA 06129 are from Day et al., 2009, Brachina and Zag from Day et al., 2012, and ALHA 77257 from Rankenburg et al., 2008.

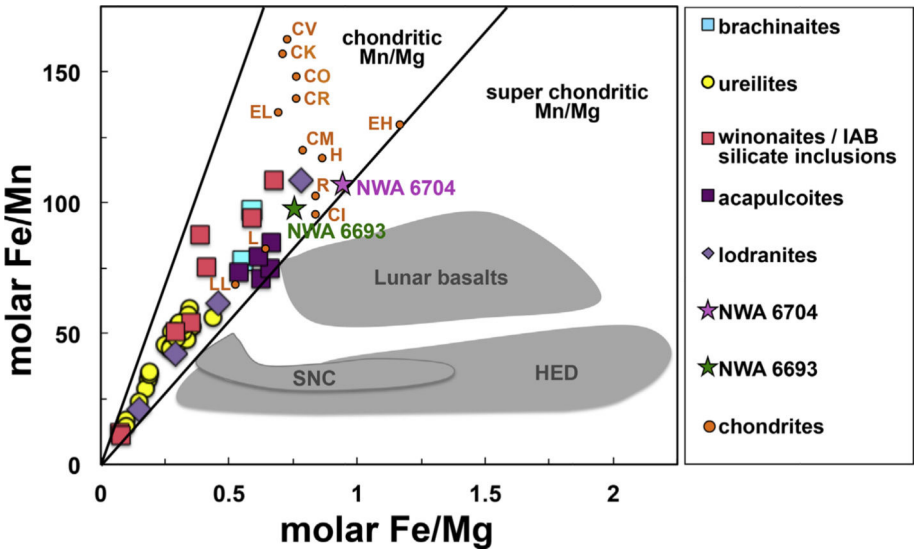


**Fig. 16.**

Plot of Fe/Mn vs. Fe/Mg, comparing NWA 6704 with chondrites, primitive achondrites, HED/SNC, and lunar basalts (Goodrich and Delaney, 2000 and the references listed there). The NWA 6704 data shown here were obtained with XRF.

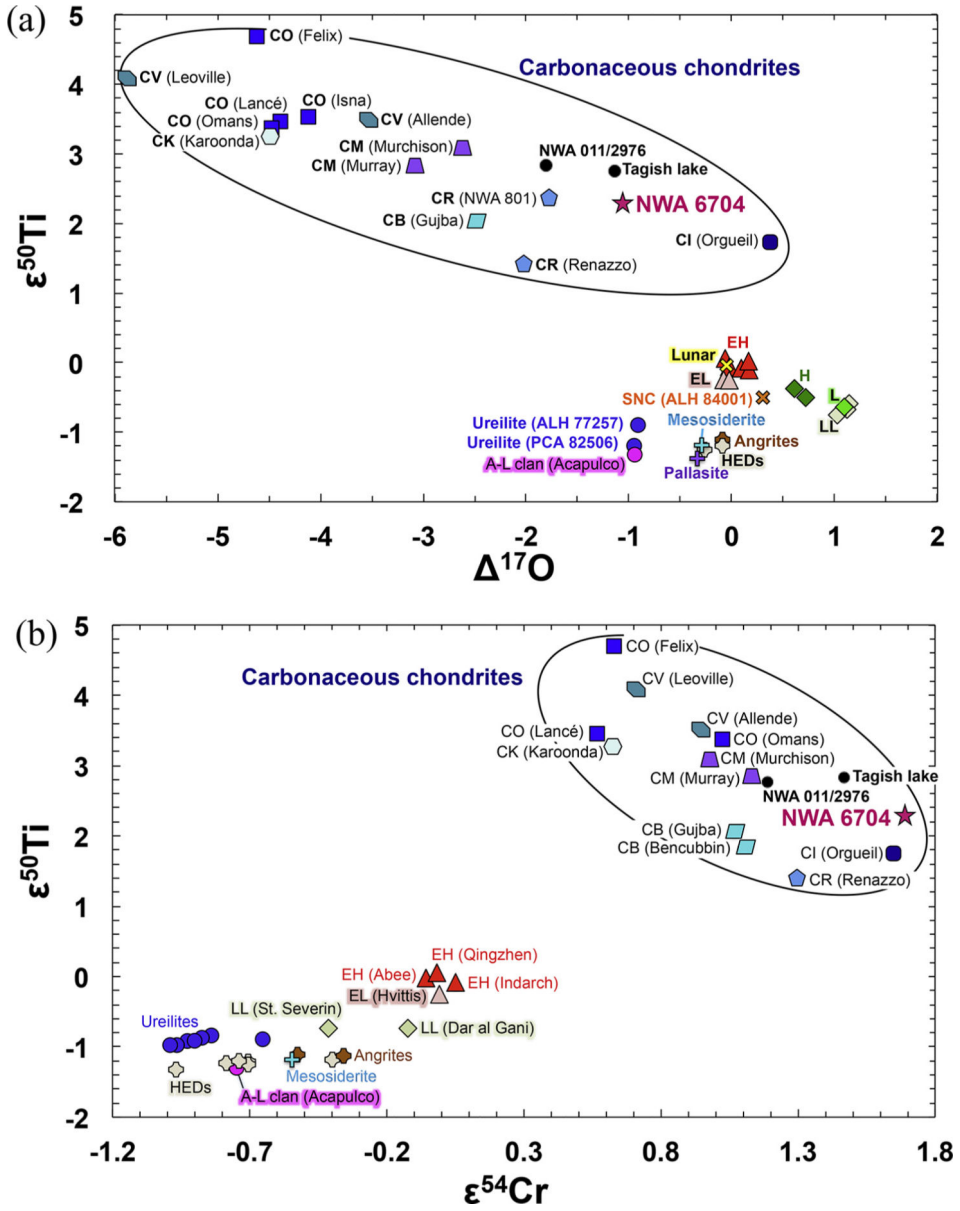


**Fig. 17.**

Comparisons of isotope compositions of NWA 6704 with planetary materials: (a) $\varepsilon^{50}$Ti vs. $\Delta^{17}$O; (b) $\varepsilon^{50}$Ti vs. $\varepsilon^{54}$Cr. Data sources are as follow: $\Delta^{17}$O, Clayton et al. (1991), Clayton and Mayeda (1996, 1999), Franchi et al. (1999), Newton et al. (2000), Greenwood and Franchi (2004), Greenwood et al. (2005, 2010, 2012), Wiechert et al. (2001, 2004), Scott et al. (2009), Schrader et al. (2011) and Harju et al. (2014); for $\varepsilon^{50}$Ti, Trinquier et al. (2007, 2008, 2009), Leya et al. (2008), Qin et al. (2010a,b) Yamakawa et al., (2010) and Zhang et al. (2012); $\varepsilon^{54}$Cr, Yamashita et al. (2005), Shukolyukov and Lugmair (2006a,b), Trinquier et al. (2007), Shukolyukov et al. (2009, 2011), Qin et al. (2010a,b), Göpel and Birck, (2010), Yamakawa et al., (2010), Larsen et al. (2011), Petitat et al. (2011), Qin et al. (2011), Sanborn et al. (2014), Bonnand et al. (2016), Göpel et al. (2015), Sanborn and Yin (2015), Schmitz et al. (2016) and Schoenberg et al. (2016).

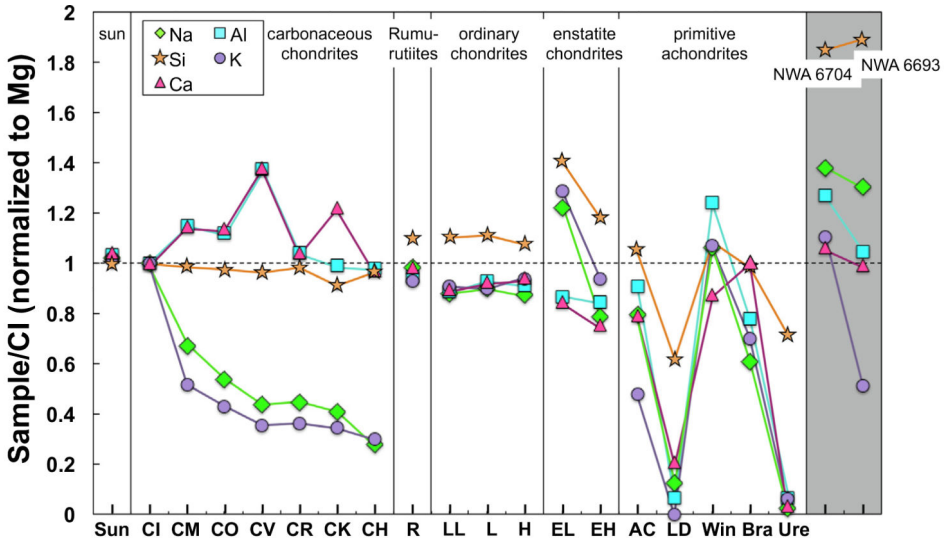


**Fig. 18.**

Mg and CI-normalized whole rock elemental abundances of NWA 6704 (XRF data in Table 4), compared with those of Sun (Palme and Beer, 1993), various chondrites (CI, CM, CO, CV, CR, CK, CH, LL, L, H, EH and EL from Wasson and Kallemeyn, 1988; R from Schulze et al., 1994) and primitive achondrites (Acapulcoite from Palme, 1981; Lodranite and Brachinite from Mittlefehldt et al., 1998; Winonaite from Graham et al., 1977; Ureilite from Wiik, 1972; NWA 6693 from Warren et al., 2013).

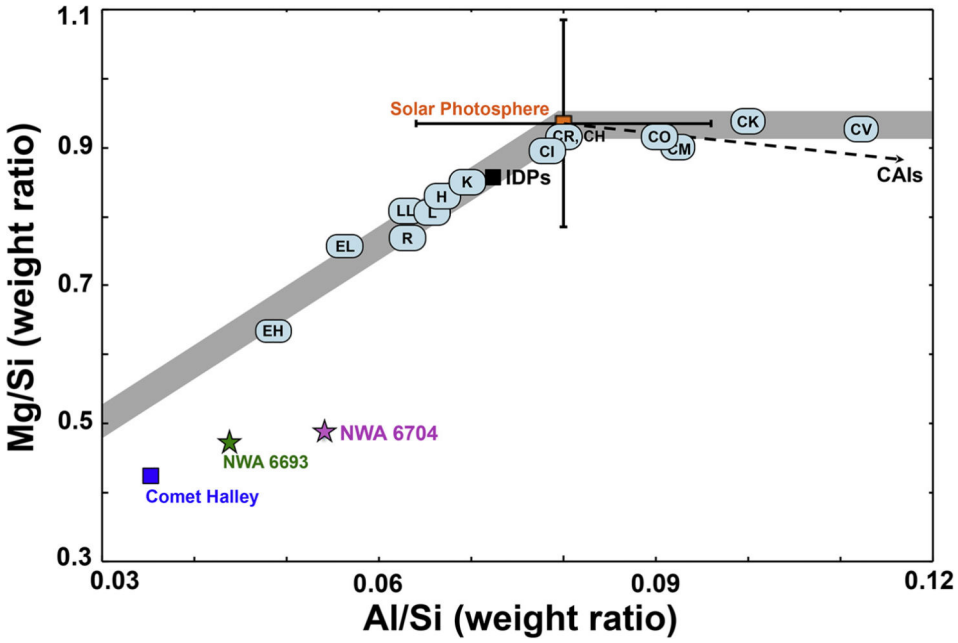


**Fig. 19.**

Plot of Mg/Si vs. Al/Si diagram, comparing NWA 6704 (XRF data in Table 4) with solar photosphere, chondrites, primitive materials (IDPs from Schramm et al., 1989; Comet's Halley dust from Jessberger et al., 1988), and NWA 6693 (Warren et al., 2013). The gray bars show two distinct trends intersect at solar composition; one is defined by carbonacous chondrites, and the other by non-carbonaceous chondrites.

**Table 1**

Summary of six NWA 6704 fragments used for petrologic studies.

| **Fragments** | **#1** | | **#2** | | | **#3** | | **#4** | | **#5** | **#6** |
|---|---|---|---|---|---|---|---|---|---|---|---|
| Thin section number | TS-1 | TS-2 | TS-3 | TS-4 | TS-5 | TS-6 | TS-8 | TS-7 | TS-9 | — | — |
| Lithology | Fine | Coarse | Coarse | Coarse | Coarse | Fine | Fine | Coarse | Coarse | — | — |
| Optical microscopy/SEM observation | ○ | ○ | ○ | ○ | ○ | ○ | ○ | ○ | ○ | × | × |
| Major element composition of minerals (EPMA) | ○ | ○ | ○ | ○ | ○ | ○ | ○ | ○ | ○ | × | × |
| Crystallographic orientations (EBSD) | × | × | × | × | × | ○ | × | ○ | × | × | × |
| Solution-based bulk chemistry (ICP-MS) | × | × | × | × | × | ○ | ○ | × | × | × | ○ |
| Whole rock major element geochemistry (XRF) | × | × | × | × | × | × | × | × | × | ○ | × |
| Elemental maps (EPMA) | × | × | × | × | × | ○ | ○ | ○ | ○ | × | × |
| Diameter of the electron probe spot | | | | | | φ26 μm | φ25 μm | φ28 μm | φ23 μm | | |
| The number of mapping points | | | | | | 700 × 1000 | 645 × 1000 | 750 × 1000 | 790 ×1000 | | |
| The mapped area | | | | | | 18 mm × 26 mm | 18 mm ×28 mm | 21 mm × 28 mm | 22 mm × 28 mm | | |
| Measured time | | | | | | 45 h | 43.5 h | 48 h | 44 h | | |

**Table 2**

Modal mineralogy of NWA 6704 thin sections (in vol.%).

| vol.% | TS-6 | TS-7 |
|---|---|---|
| Orthopyroxene | 68.7 | 69.9 |
| Olivine | 14.0 | 11.6 |
| Plagioclase | 9.9 | 11.1 |
| Pigeonite | 6.9 | 7.0 |
| Metal | 0.34 | 0.27 |
| Spinel | 0.16 | 0.14 |
| Phosphate | 0.06 | 0.05 |
| Sulfide | Minor | Minor |
| Total | 100.06 | 100.06 |

**Table 3**

The representative EPMA data (in wt.%) for individual phases.

| | Orthopyroxene | | | | | | | Olivine | | | | Vermicular olivine | | |
|---|---|---|---|---|---|---|---|---|---|---|---|---|---|---|
| | Coarse-parts (N = 68) | 2SD | Fine-parts (N = 41) | 2SD | Relict opx in fine-parts | NWA 6693 (N = 52) | NWA 6926 (N = 14) | Coarse-parts (N = 56) | 2SD | Fine-parts (N = 24) | 2SD | Coarse-parts (N = 12) | 2SD | Fine-parts (N = 1) |
| $SiO_2$ | 52.56 | 1.16 | 52.66 | 1.16 | 53.42 | 51.98 | 52.44 | 34.28 | 0.83 | 34.46 | 0.30 | 33.67 | 0.38 | 34.00 |
| $TiO_2$ | 0.08 | 0.08 | 0.07 | 0.10 | 0.06 | 0.08 | 0.05 | 0.02 | 0.05 | 0.01 | 0.02 | | | 0.01 |
| $Al_2O_3$ | 0.11 | 0.08 | 0.14 | 0.11 | 0.21 | 0.12 | 0.09 | | | | | | | |
| $Cr_2O_3$ | 0.30 | 0.19 | 0.29 | 0.12 | 0.34 | | | | | | | | | |
| Total FeO | 25.01 | 1.66 | 24.98 | 1.51 | 22.11 | 25.06 | 25.20 | 42.05 | 1.56 | 41.53 | 0.70 | 42.71 | 0.88 | 43.50 |
| MnO | 0.28 | 0.16 | 0.28 | 0.18 | 0.24 | 0.28 | 0.28 | 0.30 | 0.11 | 0.28 | 0.05 | 0.30 | 0.06 | 0.35 |
| MgO | 19.26 | 1.01 | 19.23 | 1.04 | 22.65 | 20.07 | 20.04 | 21.98 | 1.00 | 22.50 | 0.38 | 19.90 | 0.14 | 20.26 |
| NiO | 0.34 | 0.14 | 0.28 | 0.14 | 0.26 | | | 0.97 | 0.13 | 0.87 | | 0.96 | 0.08 | 0.96 |
| CaO | 1.52 | 0.71 | 1.62 | 0.54 | 0.40 | 1.58 | 1.61 | 0.08 | 0.06 | 0.08 | 0.03 | 0.06 | 0.04 | 0.04 |
| Na2O | 0.09 | 0.06 | 0.10 | 0.07 | 0.04 | 0.09 | 0.10 | | | | | 0.02 | 0.02 | 0.03 |
| $K_2O$ | | | | | | | 0.02 | | | | | | | |
| Total | 99.54 | | 99.62 | | 99.73 | 99.26 | 99.83 | 99.78 | | 99.81 | | 97.62 | | 99.15 |
| En | 56.02 | | 55.88 | | 64.1 | 56.9 | 56.7 | | | | | | | |
| Fs | 40.80 | | 40.73 | | 35.1 | 39.9 | 40.0 | | | | | | | |
| Wo | 3.17 | | 3.38 | | 0.81 | 3.21 | 3.27 | | | | | | | |
| *mg* | 57.79 | | 57.94 | | 64.6 | 58.8 | 58.6 | 48.19 | | 49.12 | | 45.4 | | 45.4 |

| | Chromite | | | | | Plagioclase | | | | | | Merrillite | | |
|---|---|---|---|---|---|---|---|---|---|---|---|---|---|---|
| | Coarse-parts (N = 38) | 2SD | Fine-parts (N = 19) | 2SD | NWA 6693 | Coarse-parts (N = 31) | 2SD | Fine-parts (N = 11) | 2SD | NWA 6693 | NWA 6926 | Fine-parts (N = 17) | 2SD | NWA 6693 (End 1) |
| $SiO_2$ | | | | | 0.03 | 66.80 | 1.80 | 67.20 | 0.81 | 66.60 | 67.60 | 0.11 | 0.04 | 0.08 |
| $TiO_2$ | 2.54 | 0.73 | 2.93 | 0.97 | 2.73 | | | | | 0.04 | 0.05 | | | 0.01 |
| $Al_2O_3$ | 2.88 | 1.59 | 2.47 | 0.82 | 2.84 | 19.38 | 0.61 | 20.07 | 0.38 | 20.09 | 18.94 | 0.02 | 0.02 | 0.01 |
| $Cr_2O_3$ | 58.32 | 1.40 | 57.99 | 2.15 | 57.89 | | | | | 0.02 | 0.04 | | | 0.01 |

| | | | | | | | | | | | | | | | |
|---|---|---|---|---|---|---|---|---|---|---|---|---|---|---|---|
| Total $Fe_2O_3$ | 2.21 | 0.96 | 2.25 | 1.00 | 2.10 | | | | | | | | | | |
| Total FeO | 31.89 | 1.33 | 32.17 | 1.02 | 31.97 | | 0.26 | 0.21 | 0.25 | 0.19 | 0.27 | 0.39 | 1.33 | 0.18 | 1.58 |
| MnO | 0.26 | 0.13 | 0.27 | 0.13 | 0.34 | | | | | | 0.01 | 0.02 | 0.03 | 0.02 | 0.01 |
| MgO | 1.54 | 0.42 | 1.54 | 0.36 | 1.73 | | | | | | 0.01 | 0.01 | 3.16 | 0.11 | 3.06 |
| NiO | 0.27 | 0.11 | 0.26 | 0.08 | | | | | | | | | | | |
| CaO | | | | | 0.02 | | 0.65 | 0.18 | 1.23 | 0.22 | 0.61 | 0.44 | 47.02 | 0.25 | 45.95 |
| $Na_2O$ | | | | | 0.02 | | 10.52 | 0.72 | 10.91 | 0.71 | 10.69 | 11.14 | 2.50 | 0.13 | 2.64 |
| $K_2O$ | | | | | | | 0.67 | 0.09 | 0.42 | 0.11 | 1.01 | 0.89 | 0.03 | 0.02 | |
| $P_2O_5$ | | | | | | | | | | | | | 46.70 | 0.34 | 45.90 |
| Total | 99.67 | | 99.65 | | 97.57 | | 98.28 | | 100.08 | | 99.35 | 99.52 | 100.90 | | 99.25 |
| Cr/(Cr + Al) | 0.93 | | 0.94 | | 0.93 | An | 3.17 | | 2.33 | | 2.90 | 2.02 | | | |
| | | | | | | Ab | 92.9 | | 92.0 | | 91.4 | 93.1 | | | |
| | | | | | | Or | 3.90 | | 5.72 | | 5.66 | 4.91 | | | |

| | Glass inclusion | | | | | Awaruite | | | | | | Pentlandite | Heazlewoodite |
|---|---|---|---|---|---|---|---|---|---|---|---|---|---|
| | In olivine | In olivine K-rich | In chromite | NWA 6693 (in chromite) | | Coarse-part (N = 18) | 2SD | Fine-parts (N = 18) | 2SD | NWA 6693 | | Coarse-parts (N = 1 | Coarse-parts (N = 1) |
| $SiO_2$ | 82.53 | 78.05 | 60.31 | 60.31 | Si | | | | | 0.02 | Si | 0.07 | 0.27 |
| $TiO_2$ | 0.08 | 0.18 | 1.01 | 1.01 | S | | | | | 0.02 | S | 47.49 | 41.9 |
| $Al_2O_3$ | 12.79 | 13.42 | 12.20 | 12.20 | Fe | 19.49 | 1.24 | 20.21 | 1.83 | 18.61 | Fe | 26.4 | 3.05 |
| $Cr_2O_3$ | | | 10.17 | 10.17 | Ni | 79.72 | 1.29 | 78.97 | 1.78 | 80.74 | Ni | 24.4 | 54.7 |
| Total FeO | 0.76 | 1.04 | 8.25 | 8.25 | Cr | | | | | | Cr | 0.02 | |
| MgO | 0.03 | 0.16 | 0.46 | 0.46 | Co | 0.71 | 0.07 | 0.74 | 0.12 | 0.74 | Co | 1.62 | 0.03 |
| NiO | 0.03 | 0.03 | 0.04 | 0.04 | | | | | | | | | |
| CaO | 0.02 | 0.02 | 0.06 | 0.06 | | | | | | | | | |
| $Na_2O$ | 3.35 | 0.81 | 7.85 | 7.85 | | | | | | | | | |
| $K_2O$ | 1.06 | 7.66 | 0.12 | 0.12 | | | | | | | | | |
| Total | 100.65 | 101.37 | 100.47 | 100.47 | Total | 99.92 | | 99.92 | | 100.13 | Total | 100.00 | 99.95 |
| An | 0.33 | 0.20 | 0.42 | 0.42 | | | | | | | | | |
| Ab | 82.4 | 13.8 | 98.6 | 98.6 | | | | | | | | | |
| Or | 17.2 | 86.0 | 1.01 | 1.01 | | | | | | | | | |

| | | | | |
|---|---|---|---|---|
| Total cations (O = 8) | 4.42 | 4.56 | 4.99 | 4.99 |

**Table 4a**

Major element abundances determined in NWA 6704 by X-ray fluorescence.

| | | NWA 6704 XRF data | NWA 6704 estimated from EPMA | NWA 6693[a] |
|---|---|---|---|---|
| $SiO_2$ | wt% | 45.75 | 52.02 | 50.52 |
| $TiO_2$ | wt% | 0.07 | 0.07 | 0.06 |
| $Al_2O_3$ | wt% | 2.18 | 1.75 | 1.94 |
| $Cr_2O_3$ | wt% | 1.00 | 0.34 | 0.44 |
| Total FeO | wt% | 28.94 | 24.78 | 24.65 |
| MnO | wt% | 0.27 | 0.26 | 0.25 |
| MgO | wt% | 17.10 | 18.29 | 18.46 |
| CaO | wt% | 1.46 | 1.27 | 1.47 |
| $Na_2O$ | wt% | 1.00 | 0.50 | 1.02 |
| $K_2O$ | wt% | 0.08 | – | 0.04 |
| $P_2O_5$ | wt% | 0.22 | 0.02 | 0.09 |

[a]NWA 6693 values from Warren et al. (2013).

**Table 4b**

Major and trace element abundances determined in NWA 6704 and NWA 6693 by ICPMS.

| **Sample** | | **NWA 6704-#3-a** | **NWA 6704-#3-b** | **NWA 6704-#3-c** | **NWA 6704-#3-ave** | **NWA 6704-#6** | **NWA 6704-#6 Plagioclase** | **NWA 6704-#6 Pyroxene** | **[a] NWA6704- J.B.** | **NWA 6693** |
|---|---|---|---|---|---|---|---|---|---|---|
| **Mass** | | **50.2 mg** | **50.1 mg** | **51.6 mg** | | **32.91 mg** | | | **125 mg** | **39.48 mg** |
| Na | wt% | | | | | 0.79 | 8.44 | 0.22 | 0.65 | 0.80 |
| Mg | wt% | | | | | 8.89 | 0.41 | 11.87 | 11.28 | 7.81 |
| Al | wt% | | | | | 0.88 | 11.78 | 0.19 | 0.97 | 0.90 |
| Ca | wt% | | | | | 1.09 | 1.20 | 1.31 | 0.99 | 1.19 |
| Cr | wt% | | | | | 0.22 | 0.01 | 0.20 | 0.16 | 0.37 |
| Fe | wt% | | | | | 20.54 | 0.73 | 20.57 | 20.85 | 18.26 |
| Ni | wt% | | | | | 1.34 | | | 0.91 | 0.58 |
| Li | μg/g | 2.091 | 2.194 | 1.883 | 2.056 | 2.709 | 0.323 | 2.607 | 3.15 | 2.574 |
| Be | μg/g | 0.025 | 0.040 | 0.017 | 0.027 | 0.008 | 0.112 | 0.025 | 0.034 | 0.018 |
| Sc | μg/g | 3.256 | 3.366 | 2.811 | 3.144 | 3.857 | | | 4.16 | 4.052 |
| Ti | μg/g | | | | | 363.68 | 221.2 | 466.2 | 351.00 | 412.69 |
| Mn | μg/g | | | | | 1900.0 | 71.4 | 2085.6 | 1814 | 1765.4 |
| V | μg/g | | | | | 64.80 | 1.8 | 46.2 | 60.3 | 74.75 |
| Co | μg/g | | | | | 554.13 | 15.5 | 365.2 | 627 | 433.84 |
| Cu | μg/g | 11.32 | 13.10 | 13.38 | 12.60 | 53.36 | 2.04 | 2.84 | 96 | 18.28 |
| Rb | μg/g | 0.377 | 0.393 | 0.328 | 0.366 | 0.164 | 3.547 | 0.268 | 0.95 | 0.529 |
| Sr | μg/g | 14.39 | 14.98 | 12.62 | 13.99 | 4.165 | 185.9 | 1.185 | 4.38 | 6.139 |
| Y | μg/g | 0.700 | 0.734 | 0.624 | 0.686 | 0.648 | 0.365 | 0.645 | 0.79 | 0.799 |
| Zr | μg/g | 2.620 | 2.762 | 2.317 | 2.566 | 0.432 | 0.900 | 2.381 | 2.52 | 3.390 |
| Nb | μg/g | 0.259 | 0.274 | 0.222 | 0.251 | 0.277 | 0.046 | 0.455 | 0.38 | 0.273 |
| Mo | μg/g | | | | | 4.374 | | | | 3.559 |
| Sn | μg/g | | | | | 0.073 | | | | 0.098 |
| Te | μg/g | | | | | 0.002 | | | | 0.008 |
| Cs | μg/g | 0.015 | 0.016 | 0.013 | 0.014 | 0.008 | | | 0.020 | 0.008 |
| Ba | μg/g | 5.402 | 5.664 | 4.794 | 5.287 | 1.575 | | | 5.21 | 5.765 |
| La | μg/g | 0.216 | 0.226 | 0.193 | 0.212 | 0.071 | 0.275 | 0.018 | 0.130 | 0.171 |
| Ce | μg/g | 0.593 | 0.620 | 0.531 | 0.581 | 0.211 | 0.668 | 0.067 | 0.336 | 0.449 |

| Sample | | NWA 6704-#3-a | NWA 6704-#3-b | NWA 6704-#3-c | NWA 6704-#3-ave | NWA 6704-#6 | NWA 6704-#6 Plagioclase | NWA 6704-#6 Pyroxene | [a]NWA6704- J.B. | NWA 6693 |
|---|---|---|---|---|---|---|---|---|---|---|
| **Mass** | | **50.2 mg** | **50.1 mg** | **51.6 mg** | | **32.91 mg** | | | **125 mg** | **39.48 mg** |
| Pr | μg/g | 0.088 | 0.093 | 0.080 | 0.087 | 0.032 | 0.091 | 0.010 | 0.0498 | 0.063 |
| Nd | μg/g | 0.421 | 0.442 | 0.377 | 0.414 | 0.164 | 0.436 | 0.063 | 0.240 | 0.301 |
| Sm | μg/g | 0.130 | 0.136 | 0.117 | 0.128 | 0.065 | 0.119 | 0.039 | 0.0880 | 0.103 |
| Eu | μg/g | 0.045 | 0.047 | 0.041 | 0.044 | 0.018 | 0.435 | 0.011 | 0.0267 | 0.031 |
| Gd | μg/g | 0.122 | 0.128 | 0.108 | 0.119 | 0.065 | 0.101 | 0.051 | 0.0994 | 0.100 |
| Tb | μg/g | 0.021 | 0.023 | 0.019 | 0.021 | 0.015 | 0.015 | 0.013 | 0.0201 | 0.021 |
| Dy | μg/g | 0.140 | 0.148 | 0.126 | 0.138 | 0.119 | 0.083 | 0.111 | 0.138 | 0.150 |
| Ho | μg/g | 0.028 | 0.029 | 0.025 | 0.028 | 0.026 | 0.014 | 0.025 | 0.0299 | 0.032 |
| Er | μg/g | 0.079 | 0.083 | 0.071 | 0.077 | 0.074 | 0.032 | 0.076 | 0.0869 | 0.090 |
| Tm | μg/g | 0.012 | 0.012 | 0.010 | 0.011 | 0.013 | 0.005 | 0.015 | | 0.015 |
| Yb | μg/g | 0.076 | 0.079 | 0.069 | 0.075 | 0.087 | 0.024 | 0.101 | 0.0917 | 0.098 |
| Lu | μg/g | 0.010 | 0.011 | 0.009 | 0.010 | 0.012 | 0.003 | 0.015 | 0.0119 | 0.013 |
| Hf | μg/g | 0.072 | 0.076 | 0.066 | 0.071 | 0.023 | 0.063 | 0.055 | 0.0573 | 0.065 |
| Ta | μg/g | 0.021 | 0.017 | 0.013 | 0.017 | 0.011 | 0.005 | 0.013 | 0.0149 | 0.012 |
| W | μg/g | | | | | 0.598 | | | 0.18 | 0.164 |
| Tl | μg/g | | | | | 0.001 | 0.001 | 0.000 | | 0.001 |
| Pb | μg/g | 0.034 | 0.031 | 0.033 | 0.033 | 0.152 | 0.056 | 0.033 | 0.013 | 0.041 |
| Th | μg/g | 0.029 | 0.029 | 0.026 | 0.028 | 0.011 | 0.024 | 0.016 | 0.0193 | 0.018 |
| U | μg/g | 0.017 | 0.017 | 0.015 | 0.016 | 0.012 | 0.010 | 0.008 | 0.0165 | 0.014 |

[a]Data provided by Jean-Alix Barrat.

**Table 5**

Highly siderophile element abundances (ppb) and $^{187}Re–^{187}Os$ systematics of NWA 6704 metal, silicate, and bulk fractions.

| Sample | Weight (mg) | Re | Os | Ir | Ru | Pt | Pd |
|---|---|---|---|---|---|---|---|
| *NWA 6704* | | | | | | | |
| Bulk A | 33.9 | 10.69 | 89.22 | 93.64 | 188.5 | 243.2 | 137.4 |
| Bulk B | 20.3 | 11.69 | 85.78 | 85.49 | 177.3 | 231.3 | 142.6 |
| Bulk C | 5.14 | 215.7 | 3242 | 2252 | 2668 | 4200 | 4064 |
| Bulk D | 6.34 | 70.99 | 694.2 | 486.6 | 725.3 | 1135 | 1188 |
| Metal | 6.02 | 3034 | 29,820 | 22,000 | 32,340 | 49,270 | 58,560 |
| Silicate | 9.96 | 1.474 | 15.42 | 23.47 | 58.37 | 48.38 | 20.36 |
| Sample | $^{187}Re/^{188}Os$ | 2 σ [b] | $^{187}Os/^{188}Os$ | 2 σ [b] | ΔOs[a] | 2 σ [b] | |
| *NWA 6704* | | | | | | | |
| Bulk A | 0.5782 | 0.0008 | 0.14133 | 0.00008 | 4.3 | 0.7 | |
| Bulk B | 0.658 | 0.0016 | 0.14738 | 0.00012 | 1.8 | 1.2 | |
| Bulk C | 0.3203 | 0.0026 | 0.12119 | 0.00076 | 6.8 | 2.2 | |
| Bulk D | 0.4932 | 0.0032 | 0.13439 | 0.00025 | 2.1 | 2.5 | |
| Metal | 0.4906 | 0.0005 | 0.13405 | 0.00018 | 0.85 | 0.4 | |
| Silicate | 0.461 | 0.013 | 0.12923 | 0.00086 | −24 | 10 | |

[a] $\Delta Os$ is the deviation in parts per 10,000, from a primordial 4568 Ma reference isochron.

[b] Uncertainties of $^{187}Re/^{188}Os$, $^{187}Os/^{188}Os$, and $\Delta Os$ are 2σ.

*Geochim Cosmochim Acta*. Author manuscript; available in PMC 2020 January 15.

**Table 6**

The oxygen isotope composition of NWA 6704 bulk meteorite, compared with those of paired meteorites.

| Sample | $\delta^{18}O$ | $\delta^{17}O$ | $\delta^{17}O^*$ | $\Delta^{17}O$[b] |
|---|---|---|---|---|
| NWA 6704 fraction-1 | 4.557 ± 0.004[a] | 1.307 ±0.007 | 1.346 | −1.051 ±0.008 |
| NWA 6704 fraction-2 | 4.637 ± 0.002 | 1.348 ±0.011 | 1.387 | −1.052 ±0.010 |
| NWA 6704 fraction-3 | 4.601 ± 0.005 | 1.327 ±0.010 | 1.366 | −1.054 ±0.009 |
| NWA 6704 fraction-4 | 4.460 ± 0.004 | 1.257 ±0.007 | 1.296 | −1.050 ±0.007 |
| NWA 6704 fraction-5 | 4.501 ± 0.004 | 1.275 ±0.006 | 1.314 | −1.053 ±0.007 |
| Average ± 2SD | 4.551 ±0.144 | 1.303 ± 0.074 | 1.342 | −1.052 ±0.004 |
| NWA 6704 (N = 2)[c] | 3.77 | | 0.95 | −1.03 |
| NWA 6693 (N = 2)[d] | 4.32 | | 1.19 | −1.08 |

[a] Uncertainties in each fraction are internal precisions and expressed as 1SE.

[b] $\Delta^{17}O = 10^3 \times [\ln(\delta^{17}O^* \times 10^{-3} + 1) - 0.527 \times \ln(\delta^{18}O \times 10^{-3} + 1)]$, where $\delta^{17}O^* = \delta^{17}O + 0.039$ (Pack et al., 2016).

[c] From Irving et al. (2011). Average and external precision of the standard during analysis was $\delta^{18}O = 5.976 \pm 0.090$, $\delta^{17}O^* = 3.140 \pm 0.144$ and $\Delta^{17}O = {}^{-}0.005 \pm 0.040$ (N = 6, 2 SD) for MSG-1 (see Tanaka and Nakamura, 2013 in detail).

[d] From Warren et al. (2013).

**Table 7**

Ti isotope data for chromite fractions of NWA 6704 and terrestrial materials.

| | $\varepsilon^{46}$Ti (2σ)[a] | $\varepsilon^{48}$Ti (2σ)[a] | $\varepsilon^{50}$Ti (2σ)[a] |
|---|---|---|---|
| *NWA 6704* | | | |
| Chromite fraction 1 | | | |
| −1 | 0.09 ± 0.30 | 0.69 ± 0.36 | 2.37 ± 0.71 |
| −2 | 0.24 ±0.32 | 0.53 ± 0.40 | 2.31 ± 0.72 |
| −3 | −0.14 ±0.35 | 0.29 ± 0.21 | 2.26 ± 0.59 |
| −4 | −0.31 ± 0.32 | 0.08 ±0.21 | 2.12 ±0.54 |
| Chromite fraction 2 | | | |
| −1 | 0.02 ± 0.26 | 0.02 ±0.35 | 2.16 ±0.71 |
| −2 | 0.19 ±0.29 | 0.11 ±0.35 | 2.19 ±0.70 |
| −3 | 0.16 ±0.27 | −0.01 ± 0.35 | 2.44 ± 0.70 |
| −4 | 0.21 ± 0.29 | −0.04 ±0.35 | 2.39 ± 0.71 |
| Average ± 2SD | 0.06 ± 0.39 | −0.21 ± 0.54 | 2.28 ± 0.23 |
| *AATS*[b] | 0.04 ± 0.25 | −0.04 ± 0.25 | 0.08 ± 0.38 |
| *SRM 3162a & 979*[c] | 0.12 ±0.30 | 0.01 ± 0.05 | 0.20 ± 0.21 |
| *BCR-2* | −0.17 ±0.30 | −0.02 ±0.31 | −0.10 ±0.32 |

[a]Uncertainties in each fraction combine the internal uncertainties and the reproducibility of the standard analyses (2 S.D.) in quadrature.

[b]Alfa Aeser Ti solution.

[c]NIST 3162a Ti solution doped with NIST 979 Cr solution, which was processed for the chemical separation before isotope analysis.